CORA Cork Open Research Archive
Cartlann Taighde Oscailte Chorcaí

Title	Pulsar discoveries from the TRAPUM UHF survey of Fermi-LAT sources
Authors	Thongmeearkom, T.;Clark, C.J.;Breton, R.P.;Burgay, M.;Nieder, L.;Dodge, O.G.;McGloughlin, B.;Barr, E.D.;Buchner, S.;Stappers, B.W.;Berteaud, J.;Ferrara, E.C.;Freire, P.C.C.;Levin, L.;Ransom, S.M.;Vleeschower, L.;Belmonte Díaz, S.;Calore, F.;Cognard, I.;Dhillon, V.S.;Grießmeier, J.;Karuppusamy, R.;Kennedy, Mark;Kramer, M.;Padmanabh, P.V.;Papa, M.A.;Phosrisom, A.;Steltner, B.
Publication date	2026-02-27
Original Citation	Thongmeearkom, T, Clark, C J, Breton, R P, Burgay, M, Nieder, L, Dodge, O G, McGloughlin, B, Barr, E D, Buchner, S, Stappers, B W, Berteaud, J, Ferrara, E C, Freire, P C C, Levin, L, Ransom, S M, Vleeschower, L, Belmonte Díaz, S, Calore, F, Cognard, I, Dhillon, V S, Grießmeier, J, Karuppusamy, R, Kennedy, M, Kramer, M, Padmanabh, P V, Papa, M A, Phosrisom, A & Steltner, B 2026, 'Pulsar discoveries from the TRAPUM UHF survey of Fermi-LAT sources', Monthly Notices of the Royal Astronomical Society, vol. 547, no. 4, stag406, pp. 1-19. https://doi.org/10.1093/mnras/stag406
Type of publication	Article (peer-reviewed)
Link to publisher's version	https://www.scopus.com/pages/publications/105036659853 - 10.1093/mnras/stag406https://www.scopus.com/pages/publications/105036659853?origin=resultslist
Rights	©The Author(s) 2026. Published by Oxford University Press on behalf of R oy al Astronomical Society. This is an Open Access article distributed under the terms of the Creative Commons A t tribution License (https://creativecommons.org/licenses/by/4.0/), which permits unrestricted reuse, distribution, and reproduction in any medium, provided the original work is properly cited. - https://creativecommons.org/licenses/by/4.0/
Download date	2026-10-12 06:48:15

Item downloaded from	https://hdl.handle.net/10468/18871

Monthly Notices of the ROYAL ASTRONOMICAL SOCIETY

MNRAS **547,** 1–19 (2026)
Advance Access publication 2026 February 27

https://doi.org/10.1093/mnras/stag406

Pulsar discoveries from the TRAPUM UHF survey of *Fermi*-LAT sources

T. Thongmeearkom [1,2★] C. J. Clark [3,4★] R. P. Breton [1★] M. Burgay [5] L. Nieder [3,4] O. G. Dodge [3,4,1] B. McGloughlin [3,4] E. D. Barr [6] S. Buchner [7] B. W. Stappers [1] J. Berteaud [8,9] E. C. Ferrara [9,10,8] P. C. C. Freire [6] L. Levin [1] S. M. Ransom [11] L. Vleeschower [12,1] S. Belmonte Díaz [1] F. Calore [13] I. Cognard [14,15] V. S. Dhillon [16,17] J.-M. Grießmeier [14,15] R. Karuppusamy [6] M. R. Kennedy [18,1] M. Kramer [6,1] P. V. Padmanabh [3,4] M. A. Papa [3,4] A. Phosrisom [2,1] and B. Steltner [3,4]

Affiliations are listed at the end of the paper

Accepted 2026 February 23. Received 2026 February 23; in original form 2026 January 12

ABSTRACT

The *Fermi* Large Area Telescope (LAT) provides advantages for radio pulsar searches by enabling efficient target selection. We can confidently point radio telescopes to the positions of *Fermi* unidentified gamma-ray sources that have a high probability of hosting a pulsar. As part of Transients and Pulsars with MeerKAT (TRAPUM), we conducted a survey of *Fermi*-LAT sources using the Ultra High Frequency (UHF; 544–1088 MHz) receiver of the MeerKAT radio telescope. We observed 79 sources that were identified as pulsar-like candidates using a random forest technique from the *Fermi*-LAT Fourth Source Catalogue. We observed each target for 10 min at two separate epochs. As a result, we discovered nine new millisecond pulsars (MSPs) and six slow pulsars. Based on the radio discoveries, we also searched for gamma-ray pulsations, confirming that seven of the newly discovered MSPs are associated with *Fermi*-LAT sources, and performed joint radio and gamma-ray pulsar timing. Companion mass estimates and evidence of radio eclipses indicate that among the nine MSPs there are three black widows and three redbacks. Lastly, we compared the discovered pulsars in the MeerKAT UHF survey against the previous *Fermi* sources TRAPUM survey at *L* band, concluding the superiority of UHF observations in sensitivity to fainter pulsars and in detection rate than *L* band for finding new gamma-ray MSPs.

Key words: binaries: general – pulsars: general – pulsars: individual: PSR J0657−4657, PSR J1259−8148, PSR J1346−2610, PSR J1356+0230, PSR J1712−1920, PSR J1823+1208, PSR J1831−6503, PSR J1910−5320, PSR J2029−4239 – gamma rays: stars.

1 INTRODUCTION

The *Fermi Gamma-ray Space Telescope*, launched in 2008, carries the Large Area Telescope (LAT; W. B. Atwood et al. 2009) as its main instrument. The *Fermi*-LAT has been used to observe high-energy gamma-ray phenomena involving non-thermal processes. Over the years, it has accumulated gamma-ray data resulting in the latest catalogue, the *Fermi*-LAT Fourth Source Catalogue (S. Abdollahi et al. 2020, 2022) Data Release 4 (4FGL DR4; J. Ballet et al. 2023), which contains ∼7000 gamma-ray sources, ∼300 of which are pulsars (D. A. Smith et al. 2023), and ∼2600 are unidentified sources.[1] Gamma-ray pulsars (the subject of this study) have unique gamma-ray emission characteristics, with highly curved spectra and low flux variability (P. M. Saz Parkinson et al. 2016), which distinguish them from other gamma-ray objects like active galactic nuclei (AGNs; M. Ackermann et al. 2012).

The *Fermi*-LAT unassociated sources that are localized with precisions of a few arcminutes and that have pulsar-like spectra provide optimal targets for pulsar searches. Consequently, many radio surveys have been searching for radio pulsations using these pulsar-like unassociated gamma-ray sources as targets under the *Fermi* Pulsar Search Consortium (P. S. Ray et al. 2012). This strategy has proven effective in numerous surveys using radio telescopes worldwide (e.g. P. Bangale et al. 2024; H. T. Cromartie et al. 2016; M. Kerr et al. 2012, 2025; P. Wang et al. 2021). By targeting *Fermi* gamma-ray sources, this search technique is particularly sensitive for detecting millisecond pulsars (MSPs), as they are often gamma-ray bright because of their high spin-down power. MSPs are especially important astrophysical laboratories because of their stable rotation, which enables precise timing studies. Moreover, many MSPs reside in diverse binary en-

★ E-mail: tinn@narit.or.th (TT); colin.clark@aei.mpg.de (CJC); rene.breton@manchester.ac.uk (RPB)

[1] https://fermi.gsfc.nasa.gov/ssc/data/access/lat/14yr_catalog/

© The Author(s) 2026.
Published by Oxford University Press on behalf of Royal Astronomical Society. This is an Open Access article distributed under the terms of the Creative Commons Attribution License (https://creativecommons.org/licenses/by/4.0/), which permits unrestricted reuse, distribution, and reproduction in any medium, provided the original work is properly cited.

Downloaded from https://academic.oup.com/mnras/article/547/4/stag406/8501212 by guest on 05 May 2026

vironments, which provide valuable opportunities to study binary evolution.

In particular, compact binary MSPs known as 'spider pulsars' feature an MSP with an irradiated, low-mass companion in a sub-day orbit: black widows (BWs) have an extremely low-mass, semidegenerate companion ($\ll 0.1\,M_\odot$), while redbacks (RBs) have a low-mass, non-degenerate companion (0.2-0.4 $M_\odot$; M. S. E. Roberts 2012). Some spiders appear to be intermediate between the conventional BW and RB categories, bridging the two types (e.g. PSR J1242−4712; A. Ghosh et al. 2024). Over the years, many spider systems have been discovered, helping in the development of binary evolution models (e.g. O. G. Benvenuto, M. A. De Vito & J. E. Horvath 2014; H.-L. Chen et al. 2013). As of this writing, there are 82 confirmed spider pulsars[2] (K. I. I. Koljonen & M. Linares 2025). Spider pulsars are challenging to detect as they often exhibit long radio eclipses due to intra-binary material and obstruction by the companion, which varies depending on the system structure and inclination (E. J. Polzin et al. 2018, 2019). L. Shang et al. (2024) studied the radio eclipse of PSR J1816+4510, finding that the pulse profile broadens in the eclipse region due to increased scattering. Similarly, observations of PSR J1653−0158 (L. Nieder et al. 2020b) suggest that some spider binaries are continuously obstructed by material, underscoring the value of observing across multiple wavelengths (e.g. radio and gamma rays). Examples of extreme radio-eclipsing spider systems include PSRs J1048+2339 (J. S. Deneva et al. 2016), J0212+5321 (K. I. Perez et al. 2023), and J0838−2827 (T. Thongmeearkom et al. 2024).

This paper is part of the Transients and Pulsars with MeerKAT (TRAPUM; B. Stappers & M. Kramer 2018) survey. The TRAPUM collaboration comprises several groups with varied search strategies, targeting different regions and sources across the sky to maximize the discovery of new pulsars. These groups include the Globular Clusters Working Group (A. Ridolfi et al. 2021; L. Vleeschower et al. 2024), the Nearby Galaxies Working Group (E. Carli et al. 2024; V. Prayag et al. 2024), the Supernova Remnants Working Group (J. D. Turner et al. 2024), and the *Fermi* Sources Working Group (C. J. Clark et al. 2023; T. Thongmeearkom et al. 2024). So far, 307 new pulsars[3] have been discovered by TRAPUM, and by the MPIfR-MeerKAT Galactic Plane Survey (MMGPS; P. V. Padmanabh et al. 2023), which uses the same processing infrastructure. The *Fermi* Sources Working Group has contributed 52 of these discoveries. Of these, 47 are from the shallow (10 min) surveys (C. J. Clark et al. 2023; this paper; Thongmeearkom et al. in preparation), while five pulsars are from the targeted deep (1-h) surveys (S. Belmonte Díaz et al. 2025; T. Thongmeearkom et al. 2024; Belmonte Díaz et al., in preparation).

Following the TRAPUM shallow survey for *Fermi*-LAT unassociated sources at *L* band (C. J. Clark et al. 2023), this paper presents the first shallow pulsar survey of *Fermi*-LAT sources using the MeerKAT radio telescope at Ultra High Frequency (UHF; 544–1088 MHz). We report results from 10-min observations of 79 unidentified *Fermi* gamma-ray sources (67 of which were previously observed with MeerKAT at *L* band, while 13 were newly added). We also included follow-up observations with other radio telescopes for detection confirmation and pulsar timing. Additionally, we compared the discoveries at *L* band (C. J. Clark et al. 2023) with those at UHF (this study) to inform the forthcoming surveys with MeerKAT (the expanded survey; Thongmeearkom et al. in preparation), as well as other pulsar surveys in general. The outline of this report is as follows: Section 2 describes the survey strategy, Section 3 presents the discoveries, localization, and timing, Section 4 discusses the characteristics of the discovered pulsars and compares the *L*-band and UHF surveys, and Section 5 provides a summary and future work plans.

2 SURVEY PROPERTIES

2.1 MeerKAT and TRAPUM processing infrastructure

The MeerKAT radio telescope is an interferometer array of 64 radio dishes, each with a diameter of 13.5 m, located in the Karoo, a desert region in the Northern Cape, South Africa. This region experiences very low levels of radio frequency interference (RFI). MeerKAT is equipped with three types of receivers: the UHF receiver (544–1088 MHz), the *L*-band receiver (856–1712 MHz), and the *S*-band receiver (1750–3499 MHz). At the time of this survey, only the *L*-band and UHF receivers were available. Full technical details can be found in R. S. Booth et al. (2009) and J. Jonas & MeerKAT Team (2016). In this paper, we present discoveries from the shallow survey conducted with the UHF receiver.

In this survey, we planned to use all the antennas to create coherent beams with high sensitivity and high resolution to cover our targets. However, not all antennas were available depending on the observing date. As a result, 56 or 60 antennas were utilized during the observations. These numbers respect the additional constraint of being divisible by four, as required by the beam-forming algorithm. This process is performed by the Filterbanking BeamFormer User Supplied Equipment (FBFUSE), a 32-node, GPU-based software beamformer developed by the Max Planck Institute for Radio Astronomy (e.g. E. D. Barr 2018; W. Chen et al. 2021). We used FBFUSE to form multiple coherent beams to cover the localization regions for sources from the *Fermi* catalogue. For each coherent beam, the channelized data were recorded on to a distributed file system accessible from the Accelerated Pulsar Search User Supplied Equipment (APSUSE). The number of beams was limited by the data rate that APSUSE could record (see section 2.1 of C. J. Clark et al. 2023, for more details). For this UHF survey, the 4096-channel MeerKAT F-engine was used to record all spectra for all targets. Therefore, the native time resolution (4096/544 MHz = 7.529 μs) was down sampled by a factor of 16 to provide 120 μs time resolution. Using this setup, APSUSE could record up to 480 coherent beams to cover the *Fermi*-LAT localized region of each source, though we reduced this number to 276 for most observations to ensure stability on the recording file-system. An example of beam tiling can be found in fig. 1 of C. J. Clark et al. (2023); note that the UHF tiling has fewer beams, but these are wider than in the *L*-band tiling due to the longer wavelength.

2.2 Observing strategy

As reported by M. Bailes et al. (2020), the full MeerKAT array offers a high gain ($G = 2.8\,\mathrm{K\,Jy^{-1}}$) and a low system temperature[4] ($T_{\rm sys} = 25\,\mathrm{K}$). Using the radiometer equation (D. R. Lorimer &

[2] https://astro.phys.ntnu.no/SpiderCAT/
[3] https://trapum.org/discoveries/
[4] https://skaafrica.atlassian.net/wiki/spaces/ESDKB/pages/277315585/MeerKAT + specifications

Downloaded from https://academic.oup.com/mnras/article/547/4/stag406/8501212 by guest on 05 May 2026

M. Kramer 2004) and sky temperature ($T_{\rm sky}$) estimates from the 408 MHz all-sky map (C. G. T. Haslam et al. 1982; M. Remazeilles et al. 2015), we calculated the minimum detectable flux density ($S_{\rm min}$) for each target,

$$S_{\rm min} = \frac{\mathrm{S/N}\,(T_{\rm sys} + T_{\rm sky})}{\beta\, G \sqrt{n_{\rm pol} t_{\rm obs} \mathrm{BW}}} \sqrt{\frac{W}{P - W}}\,, \quad (1)$$

where S/N is the signal-to-noise ratio, β is the correction factor due to digitization, $n_{\rm pol}$ is the number of polarizations, BW is the bandwidth, $t_{\rm obs}$ is the observing time, P is the pulsar's rotation period, and W is the pulse width. Based on these calculations (T. Thongmeearkom 2021), we selected a 10-min integration time, which provides a sensitivity comparable to that achieved by previous surveys with other telescopes (e.g. F. Camilo et al. 2015; M. J. Keith et al. 2011; S. M. Ransom et al. 2011). To further increase our chances of detecting faint or variable pulsars, each target was observed at two separate epochs. We expected that UHF observations would allow us to re-detect discoveries from the *L*-band survey and to discover dimmer pulsars, since pulsars generally have steep spectra making them brighter at lower frequencies (F. Jankowski et al. 2018). However, searching at UHF may present challenges for some MSPs, particularly eclipsing systems, as eclipses at higher frequencies are usually shorter and less opaque than those at lower frequencies (E. J. Polzin et al. 2020). Large dispersion measure (DM) smearing in UHF is more likely to broaden the pulse of a very fast pulsar compared to the DM smearing in *L* band (0.26 ms versus 0.10 ms for DM = 100 pc cm^{-3} within a channel). In addition, a pulsar's pulse profile tends to be broader at lower frequencies (e.g. F. Jankowski et al. 2018; S. Johnston et al. 2020). Despite these limitations, UHF remains a promising frequency range to explore, and in Section 4.2 we present a detailed comparison of *L* band and UHF based on the results of our survey.

2.3 Search pipeline

We used the `Peasoup` [5] GPU-accelerated pulsar search code to search all coherent tied-array and incoherent beams. This programme utilizes a Fast Fourier Transform-based acceleration search using time-domain resampling with incoherent harmonic summing (E. Barr 2020; V. Morello et al. 2019). We selected a maximum DM of 1000 pc cm^{-3} with a variable step size of 0.03–0.2 pc cm^{-3}, following the `DDplan.py` routine from `PRESTO` [6] (S. Ransom 2011). This range covers the maximum predicted DM along the line of sight for each target, as predicted by the YMW16 electron density model (J. M. Yao, R. N. Manchester & N. Wang 2017). We then chose a maximum acceleration of $|a| = 50\,\mathrm{m\,s^{-2}}$. This acceleration range covers the maximum acceleration expected from RB systems (J. Strader et al. 2019, see calculation in T. Thongmeearkom et al. 2024). After the search, the resulting candidate were folded using the PULSARX software[7] (Y. Men et al. 2023) and then scored by the Pulsar Image-based Classification System (PICS) machine learning classifier (W. W. Zhu et al. 2014). The last step is to investigate the pulsar candidates using a viewing programme such as `PSR_labeller` [8] or `Candyjar`.[9]

[5] https://github.com/ewanbarr/peasoup
[6] https://github.com/scottransom/presto
[7] https://github.com/ypmen/PulsarX
[8] https://github.com/01tinn/PSR_labeller
[9] https://github.com/vivekvenkris/CandyJar

2.4 Target selection

The target list was created using *Fermi*-LAT unidentified gamma-ray sources with pulsar-like gamma-ray spectra (high curvature significance and low variability) from the 4FGL catalogue (S. Abdollahi et al. 2020), which was the latest *Fermi*-LAT catalogue at the time the UHF survey commenced. Machine-learning classification techniques are an effective way to distinguish pulsar candidates from the population of unassociated sources, with successful results from many studies (T. Finke, M. Krämer & S. Manconi 2021; K. J. Lee et al. 2012; S. Luo et al. 2020; P. M. Saz Parkinson et al. 2016). However, the visual inspection method has also proven effective in identifying pulsar candidates (F. Camilo et al. 2015). These selection criteria stem from the fact that gamma-ray pulsars have higher curvature significance and lower variability compared to other classes of sources, such as AGNs.

We applied the Random Forest technique of C. J. Clark et al. (2023) to each unassociated source in the 4FGL catalogue (S. Abdollahi et al. 2020), which estimates the probability that a given source is a pulsar. Using this pulsar probability, we created a list of ranked unassociated sources. We then removed sources with declinations greater than 20°, due to the observing limits imposed by MeerKAT's location, and sources with Galactic latitudes within ±10° of the plane, in order to avoid the Galactic plane since this region of the sky was already covered by the MMGPS project (P. V. Padmanabh et al. 2023). Furthermore, we excluded sources whose 95 per cent confidence regions (localization from *Fermi*-LAT) had semimajor axes exceeding 7 arcmin, as this is the maximum area that can be covered in a single pointing using hundreds of coherent beams (e.g. 276, 288, or 480) with 50 per cent sensitivity overlap. For the first UHF epoch, we removed 13 confirmed pulsars from the first epoch at *L* band (C. J. Clark et al. 2023) and replaced them with 13 new sources. For the second epoch, we removed eight candidates from the first epoch of UHF as they have been discovered with MeerKAT and other telescopes (e.g. PSR J1947−1120 discovered with GBT; J. Strader et al. 2025). A list of UHF observations from the first epoch and the second epoch can be found in Tables A1 and A2, respectively.

3 RESULTS

We discovered nine MSPs and six slow pulsars. The pulse profiles of the MSPs are shown in Fig. 1, while the profiles of the slow pulsars are displayed in Fig. 2.

Seven of these nine new MSPs are confirmed to be counterparts of the targeted *Fermi*-LAT sources through the detection of gamma-ray pulsations (see Section 3.5). These MSPs have spin periods ranging from 1.81 to 5.31 ms and DMs from 10 to 126 pc cm^{-3}. One of these MSPs, PSR J2029−4239, is an isolated pulsar, while the remaining eight are binary systems. All were detected in coherent tied-array beams. At the time we conducted this survey, K.-Y. Au et al. (2023) identified that PSR J1910−5320 is a RB candidate with an orbital period $P_{\rm b}$ of 4.28 h, using Catalina Real-Time Transient Survey (S. G. Djorgovski et al. 2011) for optical light curves and the Southern Astrophysical Research (SOAR) telescope with the Goodman spectrograph (J. C. Clemens, J. A. Crain & R. Anderson 2004) for spectroscopy (see Section 3.3 and O. G. Dodge et al. 2024 for more details). Additionally, J. Tian et al. (2025) detected single pulses from an unknown Galactic source on two epochs in the incoherent beam from the same observations where we detected PSR J0657−4657, under the name MTP0066.

Downloaded from https://academic.oup.com/mnras/article/547/4/stag406/8501212 by guest on 05 May 2026

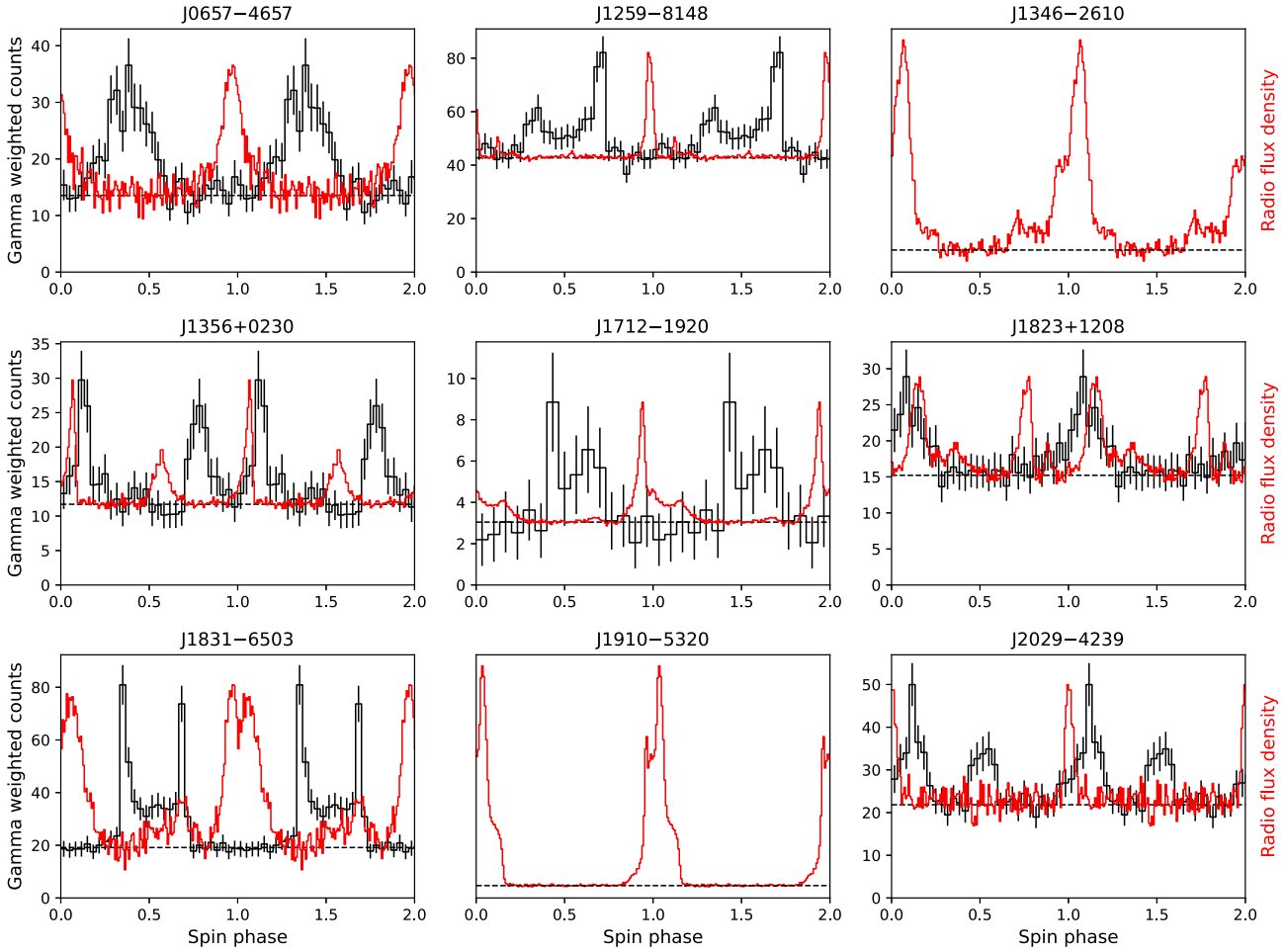

Figure 1. Radio (red) pulse profiles for all nine MSPs with phase-aligned gamma-ray (black) profiles for seven of them, showing two identical rotations for clarity. The dashed line represents the gamma-ray background level, estimated from photon weights as $b = \sum_i w_i(1 - w_i)/n_{\rm bins}$. The radio profiles are shown in arbitrary units, scaling the amplitude to match the highest gamma-ray peak and moving the baseline flux level to the gamma-ray background level.

In contrast, five of the six slow pulsars (see Section 3.6) were detected in the incoherent beam, which covers a much wider region (with FWHM of 1.9° for MeerKAT's 13.5-m antennas at the central frequency of 816 MHz), while one pulsar (PSR J1303−4713) was discovered in a coherent beam. This source was independently detected by J. Tian et al. (2025) as MTP0075.

3.1 Localization

By using the S/N values from the detection in the coherent beam and adjacent beams, a precise sky position with two-sigma localization ellipses of less than 10 arcsec can be estimated. The localization method is described in M. C. Bezuidenhout et al. (2023), which is based on the concept of M. Obrocka, B. Stappers & P. Wilkinson (2015). We used the SeeKAT package[10] on each confirmed MSP to refine each pulsar position (see section 3.2 of C. J. Clark et al. 2023, for an example). This improved positional accuracy helps us identify potential counterparts at other wavelengths and also helps in determining phase-connected timing solutions.

[10] https://github.com/BezuidenhoutMC/SeeKAT

3.2 Radio timing

Following the framework of M. Burgay et al. (2024) at L band, we initiated a follow-up timing campaign for the nine newly discovered UHF MSPs. For pulsars visible from the Northern Hemisphere, the campaign was conducted using the Nançay Radio Telescope (NRT) and the Effelsberg telescope, while for those in the Southern Hemisphere, we used the Murriyang (Parkes) telescope equipped with the Ultra-Wideband Low receiver (UWL; G. Hobbs et al. 2020). We decided on 1- to 2-h observations for follow-up sessions depending on the S/N of the discovered pulsars at MeerKAT. For fainter sources, we performed 5- or 10-min MeerKAT observations. The details of the timing observations for each source can be found in Table 1. In order to obtain an initial orbital solution, we also performed multiple 5-min MeerKAT observations with a pseudo-logarithmic cadence. In this campaign, we used the Pulsar Timing User Supplied Equipment (PTUSE; M. Bailes et al. 2020), which provides coherent de-dispersion.

Prior to obtaining a phase-connected timing solution, we obtained a preliminary timing solution for the eight binary MSPs by estimating the binary parameters, including the orbital period ($P_{\rm b}$), the epoch of ascending node ($T_{\rm asc}$), and the projected semi-major axis (x), from the observed modulation of barycentric spin

Downloaded from https://academic.oup.com/mnras/article/547/4/stag406/8501212 by guest on 05 May 2026

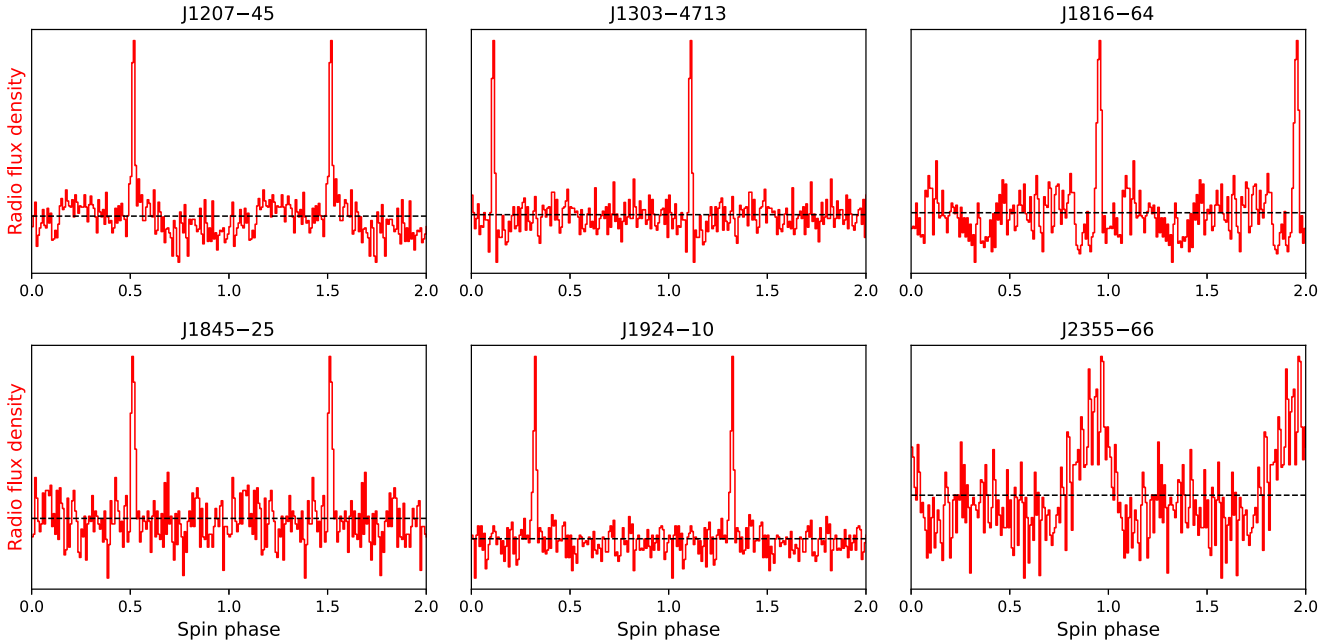

Figure 2. Radio pulse profiles for the six slow pulsars, showing two identical rotations. The profiles display the radio flux density in arbitrary units. The dashed line represents the baseline, estimated as the median of the off-pulse region.

Table 1. Parameters of the radio timing campaign of the nine newly discovered MSPs. The columns report the pulsar name, the data span of the radio timing solution, the total duration of the observations used to obtain the timing solution, and the number of ToAs that have been extracted from the observation, where each ToA corresponds to an average pulse profile over a time segment containing many individual pulses. The telescopes, from left to right, are MeerKAT (MK), Parkes (PKS), Nançay (NRT), and Effelsberg (EFF). We do not include observations with no detections in the total counts of this table.

PSR	Data span (MJD)	N. obs				t_{obs} (h)				N. ToA			
		MK	PKS	NRT	EFF	MK	PKS	NRT	EFF	MK	PKS	NRT	EFF
J0657−4657	59767–60093	8	16	–	–	1.4	22.0	–	–	46	75	–	–
J1259−8148	59536–59846	26	12	–	–	2.5	15.5	–	–	317	446	–	–
J1346−2610	60084–60185	13	–	–	–	1.0	–	–	–	192	–	–	–
J1356+0230	59674–59851	11	–	1	–	2.3	–	0.9	–	133	–	5	–
J1712−1920	60084–60258	11	21	5	7	1.1	26.6	3.8	10.7	389	205	44	74
J1823+1208	59674–60125	27	–	3	–	6.0	–	2.5	–	179	–	26	–
J1831−6503	60084–60185	11	–	–	–	2.8	–	–	–	113	–	–	–
J1910−5320	59759–60028	15	10	–	–	1.1	7.3	–	–	864	246	–	–
J2029−4239	59496–59837	4	6	–	–	0.4	3.3	–	–	44	52	–	–

periods using the standard circular-orbit relation. Subsequently, we used PRESTO 's `fit_circular_orbit.py` (S. Ransom 2011) to fit a sinusoidal modulation to the observed barycentric spin periods from multiple observations, without requiring phase alignment across observations. We then used the software TEMPO2[11] (G. B. Hobbs, R. T. Edwards & R. N. Manchester 2006) to obtain a phase-connected timing solution by flattening the residuals of the times-of-arrival (ToAs). We also added constant time offsets, referred to as 'JUMPs' to account for time delays between distinct observatories and different instruments (e.g. APSUSE, PTUSE, and other telescopes). For some binary pulsars, we employed `Dracula` [12] (P. C. C. Freire & A. Ridolfi 2018) as an additional step for determining the global rotation count and finding phase-connected timing solutions.

3.3 Spider pulsars

We found that PSRs J1259−8148, J1346−2610, J1356+0230, J1712−1920, J1831−6503, and J1910−5320 are possible spider binaries since their spin periods ($P \lesssim 5$ ms; J. Strader et al. 2019) and their orbital periods ($P_b \lesssim 1$ d; S. J. Swihart et al. 2022) lie in the range of spider pulsars. Afterwards, we became more confident in their classifications by measuring their companion masses from radio and gamma-ray timing (see Tables 2 and 3 in this work, and table 1 of O. G. Dodge et al. 2024). In addition, the RBs PSRs J1346−2610, J1712−1920, and J1910−5320, along with the BWs PSRs J1356+0230 and J1831−6503, all show evidence of radio eclipses, a characteristic signature of spider pulsars. Although PSR J1259−8148 shows no sign of radio eclipses,

[11] https://bitbucket.org/psrsoft/tempo2/src/master/
[12] https://github.com/pfreire163/Dracula

Downloaded from https://academic.oup.com/mnras/article/547/4/stag406/8501212 by guest on 05 May 2026

Table 2. Timing solutions for eight newly discovered MSPs. Timing parameters are obtained from joint radio and gamma-ray timing, as described in Sections 3.2 and 3.5. PSR J1346−2610 has only a radio timing solution, marked with an asterisk (∗), due to the absence of gamma-ray pulsations. The minimum companion mass ($M_{c,min}$) was calculated from the mass function, assuming a neutron star mass of $M_{NS} = 1.4\,M_\odot$ and an inclination of $i = 90^\circ$. We compute derived parameters from the intrinsic period derivative ($\dot{P}_{int}$). For pulsars with measured proper motions, $\dot{P}_{int}$ is obtained by correcting the observed period derivative for the Shklovskii effect (I. S. Shklovskii 1970) and Galactic acceleration (T. Damour & J. H. Taylor 1991), assuming YMW16 distances (J. M. Yao et al. 2017). For pulsars without measured proper motions, we apply only the correction for Galactic acceleration. 95 per cent upper limits on parameters are marked with a dagger (†). Timing parameter (.par) files, following the standard `tempo` format (G. B. Hobbs et al. 2006), are available as supplementary material accompanying this paper.

Parameter	PSR J0657−4657	PSR J1259−8148	PSR J1346−2610∗	PSR J1356+0230
		Timing parameters		
R.A., α (J2000)	$06^h57^m22^s.0545(3)$	$12^h59^m31^s.5832(4)$	$13^h46^m03^s.0270(6)$	$13^h56^m37^s.1262(2)$
Decl., δ (J2000)	$-46^\circ57'52''.611(5)$	$-81^\circ48'51''.3752(4)$	$-26^\circ10'18''.73(2)$	$+02^\circ30'30''.441(7)$
Proper motion in R.A., $\mu_\alpha \cos\delta$ (mas yr^{-1})	4.1 ± 3.1	-5.9 ± 0.5	–	-17.3 ± 2.1
Proper motion in Decl., μ_δ (mas yr^{-1})	2.4 ± 3.2	6.3 ± 0.3	–	-9.2 ± 5.2
DM (pc cm^{-3})	126.059(8)	44.314(7)	20.145(4)	17.787(1)
Spin frequency, ν (Hz)	253.4542797024(2)	479.4813415355(4)	361.2127648726(5)	353.7362124742(2)
Spin-down rate, $\dot{\nu}$ (Hz s^{-1})	$-4.609(9) \times 10^{-16}$	$-7.67(2) \times 10^{-16}$	$-7.0(2) \times 10^{-16}$	$-9.781(7) \times 10^{-16}$
Orbital period, P_b (d)	84.0524734(6)	0.185680580(2)	0.1577240538(2)	0.141879279(2)
Projected semimajor axis, x (lt s)	36.002523(8)	0.084884(5)	0.323356(6)	0.022654(3)
Epoch of ascending node, T_{asc} (MJD)	59825.373197(4)	59635.516072(2)	60084.9496878(4)	59674.080619(2)
1st Laplace-Lagrange parameter, ϵ_1	$8.55(6) \times 10^{-5}$	–	–	–
2nd Laplace-Lagrange parameter, ϵ_2	$-2.38(4) \times 10^{-5}$	–	–	–
		Derived parameters		
Spin period, P (ms)	3.945484768196(3)	2.0855868901959(2)	2.768451442608(4)	2.826965305603(1)
Spin period derivative, $\dot{P}$ (s s^{-1})	$7.17(1) \times 10^{-21}$	$3.3360(8) \times 10^{-21}$	$5.4(1) \times 10^{-21}$	$7.817(5) \times 10^{-21}$
Intrinsic period derivative, $\dot{P}_{int}$ (s s^{-1})	7.31×10^{-21}	3.08×10^{-21}	5.76×10^{-21}	3.77×10^{-21}
Spin-down power, $\dot{E}$ (erg s^{-1})	4.7×10^{33}	1.3×10^{34}	1.1×10^{34}	6.6×10^{33}
Surface magnetic field strength, B_S (G)	1.7×10^8	8.1×10^7	1.3×10^8	1.0×10^8
Light-cylinder magnetic field strength, B_{LC} (G)	2.6×10^4	8.2×10^4	5.6×10^4	4.3×10^4
Minimum companion mass, $M_{c,min}$ ($M_\odot$)	0.27	0.03	0.15	0.01
Eccentricity, e	$8.88^{+0.03}_{-0.08} \times 10^{-5}$	–	–	–
Proper motion, μ (mas yr^{-1})	$<11^\dagger$	8.6 ± 0.4	–	19.6 ± 3.1
Distance from YMW16 (kpc)	0.5	1.4	1.2	1.8
Distance from NE2001 (kpc)	>50.0	1.5	0.9	1.2
System class	pulsar–white dwarf	BW	RB	BW

its compact orbit and very low companion mass still suggests it is a BW rather than a He white dwarf system.

We can interrogate the companion to the neutron star in spider systems at optical wavelengths. Spider companions show characteristic sinusoidal optical variability, driven by two key mechanisms. First, due to compact orbits and tidal locking, the hemisphere of the companion facing the pulsar is heavily irradiated by the pulsar wind. This irradiated face (the dayside) becomes hotter and thus brighter than the unirradiated face (the nightside), producing a single-peaked light curve (e.g. R. P. Breton et al. 2013; P. J. Callanan, J. van Paradijs & R. Rengelink 1995), with the peak occuring when the irradiated face is presented to the observer. Secondly, the gravitational distortion of the companion leads to ellipsoidal modulation, producing a double-peaked light curve. Both effects are present in most systems, but their relative strength determines the observed morphology. In BWs, strong irradiation often dominates and masks the weaker ellipsoidal component, while in RBs, the larger and more distorted companions make the ellipsoidal modulation more prominent. However, some strongly irradiated RBs still show single-peaked, asymmetric double-peaked, or irregular light curves. For example, PSR J1910-5320 has been observed using ULTRCAM/NTT and SOAR/Goodman to obtain optical light curves and spectroscopy (O. G. Dodge et al. 2024). The study found that the optical light curves of PSR J1910−5320 display a single-peaked light curve and found that this system has a companion mass of $0.28\,M_\odot$ and a neutron star mass of $1.4\,M_\odot$, confirming its classification as an irradiated RB.

To characterize the companion in the system, PSR J1346−2610 was observed over two nights, the 18th and 19th of March 2023, with ULTRACAM (V. S. Dhillon et al. 2007). ULTRACAM, mounted on the European Southern Observatory's New Technology Telescope (NTT) at the La Silla observatory, offers high time-resolution multiband simultaneous photometry, in our case providing r_s, g_s, and u_s light curves. Here, the subscript s denotes 'Super-SDSS' filters which cover the same wavelength range as the traditional SDSS filters, but with a higher throughput (V. S. Dhillon et al. 2021). The details of the observations are shown in Table 4. The data were reduced using the HiPERCAM pipeline (V. S. Dhillon et al. 2021) following the typical process: de-biasing, flat-fielding and aperture selection. For the r_s and g_s filters, conversion from instrumental to calibrated flux required 15 nearby sources whose magnitudes are within the Pan-STARRS1 survey catalogue (K. C. Chambers et al. 2016; H. A. Flewelling et al. 2020) to be extracted alongside the target, with the same reference stars used for each night of data. As Pan-STARRS1 uses standard SDSS ($g'r'i'z'$) filters, as opposed to the HiPERCAM super-SDSS filters ($u_s g_s r_s$), we transformed the listed source magnitudes using the colour-transforms listed in A. J. Brown et al. (2022). Pan-STARRS1 does not include a u' filter, thus this simple calibration could not be used for our u_s data. Instead, we determined the instrumental zeropoint by observation of the standard stars GD

Downloaded from https://academic.oup.com/mnras/article/547/4/stag406/8501212 by guest on 05 May 2026

Table 3. Continuation of Table 2.

	PSR J1712−1920	PSR J1823+1208	PSR J1831−6503	PSR J2029−4239
	Timing parameters			
R.A., α (J2000)	$17^h12^m01^s.4376(1)$	$18^h23^m18^s.3158(3)$	$18^h31^m04^s.3241(3)$	$20^h29^m35^s.2006(9)$
Decl., δ (J2000)	$-19°20'24''.52(2)$	$+12°08'38''.715(9)$	$-65°03'13''.984(4)$	$-42°39'35''.99(2)$
Proper motion in R.A., $\mu_\alpha \cos\delta$ (mas yr^{-1})	–	9.4 ± 4.1	-5.5 ± 0.3	5.6 ± 2.8
Proper motion in Decl., μ_δ (mas yr^{-1})	–	-5.7 ± 7.9	-2.7 ± 0.6	2.8 ± 6.0
DM (pc cm^{-3})	49.4049(2)	40.687(2)	25.715(9)	10.170(2)
Spin frequency, ν (Hz)	552.2592655671(2)	192.08456416966(9)	539.62314331721(4)	188.1764568362(1)
Spin-down rate, $\dot{\nu}$ (Hz s^{-1})	$-3.03(1) \times 10^{-15}$	$-3.287(6) \times 10^{-16}$	$-5.749(2) \times 10^{-16}$	$-3.339(5) \times 10^{-16}$
Orbital period, P_b (d)	0.183439029(3)	7.79893996(4)	0.157913023(2)	–
Projected semimajor axis, x (lt s)	0.497066(7)	6.169776(4)	0.063017(3)	–
Epoch of ascending node, T_{asc} (MJD)	60084.88545055(8)	59676.197511(1)	60084.926947(3)	–
1st Laplace-Lagrange parameter, ϵ_1	$(-3.8 \pm 17) \times 10^{-6}$	$9(2) \times 10^{-6}$	$3(1) \times 10^{-4}$	–
2nd Laplace-Lagrange parameter, ϵ_2	$1.9(9) \times 10^{-5}$	$2(1) \times 10^{-6}$	$-1.5(9) \times 10^{-4}$	–
OPV amplitude, h_{opv}	–	–	−6.7(2)	–
OPV cutoff frequency, $\nu_{c,opv}$ (yr^{-1})	–	–	−1.4(6)	–
OPV spectral index, γ_{opv}	–	–	2(1)	–
	Derived parameters			
Spin period, P (ms)	1.8107437255454(5)	5.206040393317(2)	1.8531451298637(1)	5.314161063573(3)
Spin period derivative, $\dot{P}$ (s s^{-1})	$9.92(3) \times 10^{-21}$	$8.91(1) \times 10^{-21}$	$1.9742(6) \times 10^{-21}$	$9.43(1) \times 10^{-21}$
Intrinsic period derivative, $\dot{P}_{int}$ (s s^{-1})	9.87×10^{-21}	6.57×10^{-21}	1.89×10^{-21}	6.95×10^{-21}
Spin-down power, $\dot{E}$ (erg s^{-1})	6.6×10^{34}	1.8×10^{33}	1.2×10^{34}	1.8×10^{33}
Surface magnetic field strength, B_S (G)	1.4×10^8	1.9×10^8	5.9×10^7	1.9×10^8
Light-cylinder magnetic field strength, B_{LC} (G)	2.1×10^5	1.2×10^4	8.7×10^4	1.2×10^4
Minimum companion mass, $M_{c,min}$ ($M_\odot$)	0.22	0.22	0.03	–
Eccentricity, e	$<3.8 \times 10^{-5}$ †	$<1.3 \times 10^{-5}$ †	$<5.3 \times 10^{-4}$ †	–
Proper motion, μ (mas yr^{-1})	–	<21†	6.1 ± 0.4	18.5 ± 5.8
Distance from YMW16 (kpc)	1.6	1.7	1.0	0.6
Distance from NE2001 (kpc)	1.4	1.9	0.9	0.5
System class	RB	Pulsar–white dwarf	BW	Isolated pulsar

Table 4. ULTRACAM observations of PSR J1346−2610. The exposure time was 10 s, with only 24 milliseconds of dead time between each frame. To increase signal-to-noise ratio, a single u_s datapoint consists of 3 stacked exposures, resulting in the lower number of u_s datapoints.

Start time (UTC)	Length (h)	Orbital coverage	n datapoints		
			r_s	g_s	u_s
2023/03/19 04:06:28	2.25	0.01–0.60	755	798	267
2023/03/20 04:01:49	2.33	0.51–0.94	579	573	192

108 (on the first night) and GD 71 (on the second night). The reference aperture magnitudes could then be bootstrapped according to this zeropoint, and a consistent u_s reduction between nights was obtained.

We found a single-peaked light curve (Fig. 3). As described previously, this feature is more commonly seen in BWs, although some RBs also exhibit such profiles. A short orbital period of ∼3.8 h supports this BW classification, as they tend to have more compact orbits. However, the `Icarus` (see R. P. Breton et al. 2012 for details) optical modelling results presented in Table 5 strongly suggest a RB, with a companion mass of 0.23 $M_\odot$, albeit an unusually cold example. Whilst, given the lack of spectroscopy, the component masses cannot be precisely estimated, we can marginalize over the neutron star mass with a loose top-hat prior allowing for any neutron star mass in the range $1.2\,M_\odot < M_{NS} < 2.5\,M_\odot$.

By averaging the surface element temperatures over the night and daysides, (phases 0.25 and 0.75, respectively), we can characterize the temperatures of each face. The nightside temperature is low ($T_N = 2300$ K) in comparison with other field RBs

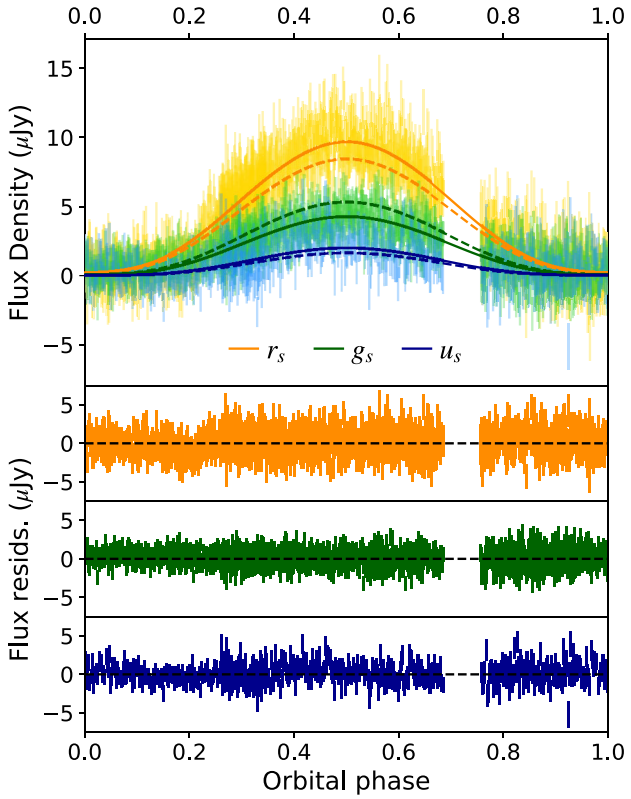

Figure 3. Optical light curves (points), `Icarus` model fits (solid lines) and resiudals (bottom panels) for PSR J1346−2610 from ULTRACAM data.

Downloaded from https://academic.oup.com/mnras/article/547/4/stag406/8501212 by guest on 05 May 2026

Table 5. Parameter estimation from optical modelling of PSR J1346−2610.

Parameter	Value
Fit parameters	
Neutron star mass, $M_{\rm NS}$ ($M_\odot$)	$1.67^{+0.5}_{-0.4}$
Reddening, $E(B-V)$	$0.0507^{+0.003}_{-0.003}$
Inclination, i (°)	49^{+9}_{-3}
Filling factor, $f_{\rm RL}$	$0.79^{+0.02}_{-0.03}$
Base temperature, $T_{\rm B}$ (K)	2400^{+800}_{-700}
Irradiation temperature, T_I (K)	6600^{+100}_{-100}
Distance, d (kpc)	$5.3^{+0.4}_{-0.4}$
Derived parameters	
Observed temperature: inferior conjunction, $T_{\rm Inf}$ (K)	2700^{+500}_{-300}
Observed temperature: superior conjunction, $T_{\rm Sup}$ (K)	5000^{+200}_{-100}
Nightside temperature, $T_{\rm N}$ (K)	2300^{+800}_{-700}
Dayside temperature, $T_{\rm D}$ (K)	5300^{+100}_{-100}
Volume averaged filling factor, $f_{\rm v}$	$0.93^{+0.02}_{-0.02}$
Mass ratio, q	$7^{+1}_{-0.9}$
Companion projected radial velocity, $K_{\rm c}$ (km s^{-1})	330^{+50}_{-40}
Companion mass, $M_{\rm c}$ ($M_\odot$)	$0.23^{+0.04}_{-0.04}$

(J. A. Simpson et al. 2025), consistent with the unusual faintness of the source. The distance determined from our modelling ($d \sim 5.3$ kpc) is also further than the expectation given the DM ($d \sim 1.2$ kpc). This discrepancy exceeds the nominal precision of electron density models, suggesting that the electron density along the line of sight has been overestimated. However, in this direction the DM quickly plateaus thus our modelled distance is not inconsistent.

3.4 Other MSPs

For PSRs J0657−4657 and J1823+1208, the orbital periods are 84.1 and 7.8 d, with companion masses of 0.28 and 0.23 $M_\odot$, respectively. These masses are consistent with those of low-mass white dwarfs (0.09–0.29 $M_\odot$; D. Mata Sánchez et al. 2020; S. J. Swihart et al. 2022). The relatively long orbital periods further suggest a binary system with a He white dwarf ($P_b \gtrsim 2$ d; T. M. Tauris & E. P. J. van den Heuvel 2023) rather than a spider binary. In contrast, PSR J2029−4239 appears to be an isolated pulsar, as there is no evidence of orbital acceleration from the radio timing observations or over the ∼16.5 yr data span used in gamma-ray timing. This lack of acceleration suggests that it does not have a close companion. Its rapid spin period ($P \sim 5.3$ ms) implies that it was likely recycled in the past through accretion in a binary system, but has since lost or ablated its companion, leaving it isolated.

3.5 Gamma-ray pulsations and timing

All MSPs discovered in this survey were found targeting a *Fermi* unidentified source, thus we performed follow-up searches for gamma-ray pulsations. Depending on the system, an initial radio timing solution spanning just a few weeks may already be sufficient to guide a successful gamma-ray follow-up search (see e.g. L. Nieder et al. 2019; P. S. Ray et al. 2022). In more complicated cases, longer radio timing solutions are required to reveal the gamma-ray pulsations (see, e.g. M. Burgay et al. 2024; T. Thongmeearkom et al. 2024).

We analysed these data following LAT standard procedures. We used 'Pass 8' `P8R3_SOURCE_V3` instrument response functions (W. Atwood et al. 2013; P. Bruel et al. 2018). Photons were selected based on their energy as described in the 4FGL-DR4 catalogue (J. Ballet et al. 2023). We assigned probability weights to these photons derived from spectral and spatial models of the gamma-ray sky (P. Bickel, B. Kleijn & J. Rice 2008; P. Bruel 2019; M. Kerr 2011), following the `gtsrcprob` routine with source positions and spectra from 4FGL DR4 (J. Ballet et al. 2023). The sky model used the `iso_P8R3_SOURCE_V3_v1.txt` isotropic diffuse emission model[13] and the rescaled[14] `gll_iem_v07` interstellar emission model (F. Acero et al. 2016) associated to the 4FGL-DR4 catalogue.

For our analyses, we chose a cut on probability weights to save computing power in searches and timing. The test statistics and especially the weighted H-test (O. C. de Jager, B. C. Raubenheimer & J. W. H. Swanepoel 1989; M. Kerr 2011) depend on these weights and scale linearly with $W^2 = \sum_j w_j^2$ (L. Nieder et al. 2020a). The proportionality factors are source-specific, depending on the pulse profile and the background level, but are typically of order unity (0.5 to 2). The cutoff weight is chosen so that most of the low-weight photons are removed while securing 99 per cent of the expected signal power typically corresponding to $w_{\rm min} \approx 0.01$-0.03.

We found gamma-ray pulsations from the two pulsars, PSRs J1823+1208 and J2029−4239 in a single fold. In these cases, the radio-timing ephemeris revealed gamma-ray pulsations over most of the *Fermi* mission without a search being required. Further tweaking of parameters like the spin-down rate $\dot{\nu}$ showed pulsations over the entire mission starting in 2008.

We found gamma-ray pulsations from the three pulsars, PSRs J0657−4657, J1259−8148, and J1356+0230 in follow-up searches. Using the radio ephemerides as starting positions, we searched for gamma-ray pulsations in the *Fermi*-LAT data over a five-dimensional parameter space (α, δ, ν, $\dot{\nu}$ and $P_{\rm b}$). For computational reasons, we truncated H at the 3rd out of 20 harmonics as pulsars have most of their Fourier power in the lowest harmonics (H. J. Pletsch & C. J. Clark 2014).

These five radio and gamma-ray pulsars were timed following the methods described in M. Burgay et al. (2024). The joint radio and gamma-ray timing code[15] uses the pulsar timing software `PINT`[16] (J. Luo et al. 2021) to fold the radio and gamma-ray data individually and joins the two standard test statistics ($\chi^2_{\rm radio}$ for radio ToAs, $\log \mathcal{L}_\gamma$ for gamma-ray photons) into a new log-likelihood function

$$\log \mathcal{L}_{\rm joint} = \log \mathcal{L}_\gamma - 0.5\chi^2_{\rm radio}\,. \quad (2)$$

The Affine Invariant Markov chain Monte Carlo (MCMC) Ensemble sampler EMCEE (D. Foreman-Mackey et al. 2013) is used to explore the parameter space. The timing solutions are presented in Tables 2 and 3.

[13] https://fermi.gsfc.nasa.gov/ssc/data/access/lat/BackgroundModels.html
[14] https://fermi.gsfc.nasa.gov/ssc/data/analysis/software/aux/4fgl/Galactic_Diffuse_Emission_Model_for_the_4FGL_Catalog_Analysis.pdf
[15] https://fermi.gsfc.nasa.gov/ssc/data/analysis/user/jrag-timing.py
[16] https://github.com/nanograv/PINT

Downloaded from https://academic.oup.com/mnras/article/547/4/stag406/8501212 by guest on 05 May 2026

Gamma-ray pulsations were only detected from the black-widow pulsar J1831−6503, after a longer radio timing campaign which revealed orbital period variations. A sliding window method revealed pulsations over the entire mission span and served as starting solution for a joint radio and gamma-ray timing analysis, treating the variations as a stationary Gaussian process (C. J. Clark et al. 2026), as has been done for previous TRAPUM spider binaries (S. Belmonte Díaz et al. 2025; M. Burgay et al. 2024; T. Thongmeearkom et al. 2024). We use a Matérn covariance function, a power-law function parametrized by three hyperparameters, amplitude ($A_{\rm opv}$), cutoff frequency ($\nu_{\rm c,opv}$) and spectral index ($\gamma_{\rm opv}$). The measured pulsar parameters are shown in Table 3, with the phase-folded gamma-ray data and the orbital period variations being depicted in Fig. B1. We did not find evidence for orbital period variations in the two other new BWs, PSRs J1259−8148, and J1356+0230.

The analysis of the three RB pulsars is hampered by their faintness in gamma rays, and the likelihood that they also exhibit orbital period variations. PSRs J1346−2610 and J1910−5320 have $W^2 = 178$ and $W^2 = 181$, respectively, which are low enough to prevent a detection if orbital period variations are present. This is certainly the case for PSR J1910−5320 where two orbital frequency derivatives were required to fit the seven months of radio ToAs. We did not detect significant gamma-ray pulsations from either pulsar when folding only data during the interval spanned by radio ToAs. For these pulsars, significant detections with $H \approx 25$ are only possible over substantially longer segments, of around 1.1-4.7 yr (depending on the source-specific proportionality factor), over which time the orbital period could vary substantially. For the RB pulsar PSR J1712−1920, folding the gamma-ray data spanned by the radio ephemeris resulted in faint, but significant pulsations with $H = 33$. We have not yet found a phase-connected timing solution spanning much more time than this. This is not unusual as it is difficult to find a timing solution for a faint ($W^2 = 140$) RB with orbital-period variations. The radio-only timing solution is shown in Table 3. All of these will require continued monitoring with radio telescopes to enable gamma-ray pulsation detections and/or a joint timing analysis.

3.6 Slow pulsars

Six slow pulsars have been found (PSRs J1207−45, J1303−4714, J1816−64, J1845−25, J1924−10, J2355−66). Five of these have been found in the incoherent beam, which has a larger field of view (FWHM ∼114 arcmin) compared to the tiling of the small coherent beams (∼7 arcmin). As a result, it is impossible to localize them like other MSP discoveries from the coherent beams. Hence, we report them with names indicating their coarse positional uncertainties. The information of these pulsars can be found in Table A3.

We find no evidence that these slow pulsars emit gamma-ray pulsations. Associations with the gamma-ray sources that were targeted during these observations can be ruled out due to the lack of detection in any of the coherent beams that were tiling the 99 per cent confidence regions. We also found no other unassociated 4FGL-DR4 sources within the FWHM of the incoherent beams around these sources. Furthermore, PSRs J1303−4713 and J1816−64 have spin periods ($P = 2.56$ s and $P = 1.22$ s, respectively) longer than that of the slowest known gamma-ray pulsar (PSR J1731−4744 with $P = 0.83$ s; D. A. Smith et al. 2019), while only 3 and 5 known gamma-ray pulsars are slower than PSRs J1845−25 and J1207−45, respectively (D. A. Smith et al. 2023). PSRs J1924−10 and J2355−66 have spin periods of about 114 and 121 ms, respectively, and could either be energetic young pulsars, or could be mildly recycled pulsars similar to PSR J1744−3922 (R. P. Breton et al. 2007). However, because of the lack of precise positions, and the very large number of observations that would be required to tile the incoherent beam FWHM with coherent beams, we deemed a dedicated follow-up investigation of these pulsars to be beyond the scope of this work.

3.7 Distance to PSR J0657−4657

The distance to a pulsar may be estimated through the measured DM and an electron density model of our galaxy. For PSR J0657−4657, the measured DM of 126 pc cm^{-3} corresponds to a distance of 0.5 kpc in the YMW16 model (J. M. Yao et al. 2017). However, the NE2001 model (J. M. Cordes & T. J. W. Lazio 2002) saturates at a DM of 81.5 pc cm^{-3} at 14 kpc along this line of sight and jumps to a distance of 50 kpc for any larger value of DM. This clearly demonstrates a limitation of the NE2001 model along this particular direction. One possible reason is that the line of sight to PSR J0657−4657 intersects the Gum Nebula, a large H II region with a distance of ∼450 pc (C. R. Purcell et al. 2015), which might not be correctly accounted for in NE2001. Similar discrepancies have been noted in other MSPs whose sight lines pass near structured ionized regions (T. Thongmeearkom et al. 2024), although the mismatch for PSR J0657−4657 appears noticeably larger.

An independent distance constraint on the distance comes from gamma-ray data. The gamma-ray flux of $F_\gamma = (2.63 \pm 0.36) \times 10^{-12}$ erg cm^{-2} s^{-1} is measured in the energy range between 100 MeV and 100 GeV from 4FGL DR4 (J. Ballet et al. 2023). Assuming a gamma-ray efficiency $\eta_\gamma = \mathcal{L}_\gamma/\dot{E} = 4\pi d^2 F_\gamma/\dot{E}$ of 100 per cent (i.e. the entire spin-down power is converted into gamma rays) gives a conservative distance upper limit of 3.8 kpc. A more realistic value is obtained assuming the canonical heuristic value of $\eta_\gamma = \sqrt{10^{33}\,\mathrm{erg\,s^{-1}}/\dot{E}}$ (e.g. D. A. Smith et al. 2023), resulting in an estimate of 2.6 kpc.

Another method exploits the correction factors on the spin-down rate $\dot{\nu}$, the Shklovskii effect (I. S. Shklovskii 1970) induced by proper motion and acceleration in the Galactic potential. These effects depend on sky position and distance and as under normal circumstances we would assume a negative $\dot{\nu}$, this may be used to set a limit. Here, this results in a limit of 32 kpc, which is less constraining than the estimates using the YMW16 model and the gamma-ray efficiency.

The range of distance estimates for PSR J0657−4657 are wide and without other options available (e.g. parallax) a reliable estimate cannot be reported. However, it is safe to assume that the NE2001 result can be ruled out and that the distance is likely smaller than 3.8 kpc.

3.8 Continuous gravitational wave searches

Gravitational wave emission is expected from non-axisymmetric neutron stars with the dominant signal frequency being equal to twice the rotational frequency of the star ($\nu_{\rm GW} = 2\nu$) (D. I. Jones 2015). The intrinsic continuous gravitational wave amplitude, h_0, crucially depends on the distance to the source and the fraction of the rotational energy being channeled into gravitational wave radiation (P. Jaranowski, A. Królak & B. F. Schutz

Downloaded from https://academic.oup.com/mnras/article/547/4/stag406/8501212 by guest on 05 May 2026

1998). In this regard, of the pulsar discoveries, PSRs J0657−4657 and J2029−4239 are the most promising sources to produce detectable continuous gravitational wave signals. We search for such signals using data from the first, second, third, and fourth observing runs of the Advanced LIGO detectors (R. Abbott et al. 2021, 2023; The LIGO Scientific Collaboration 2025) from both sources.

Since the timing solutions span all epochs from the first through to the fourth observation run, we perform a single-template targeted-search for continuous gravitational wave emission centred at twice the star's rotational frequency, using a frequentist analysis procedure based on the multidetector maximum-likelihood $\mathcal{F}$-statistic (C. Cutler & B. F. Schutz 2005). This method coherently combines data from the Hanford and Livingston Advanced LIGO detectors. The results of this search are consistent with a non-detection and we set 95 per cent confidence upper limits on the intrinsic gravitational wave amplitude h_0. We obtain upper limits on h_0 of 3.0×10^{-27} and 6.3×10^{-27} for PSRs J0657−4657 and J2029−4239, respectively.

Additionally, the gravitational wave emission may be mismatched from exactly twice the rotational frequency, motivating an additional band search around each pulsar's nominal frequency and spin-down. In the present analysis, however, the nominal gravitational wave frequency of PSR J0657−4657 lies within a frequency range for which the sensitivity of the Advanced LIGO detectors is limited due to the mirror's suspension violin modes that render a reliable band search for this pulsar infeasible. We therefore restrict this extended analysis to PSR J2029−4239 only and search in a range of $\Delta\nu_{\rm GW} = 4 \times 10^{-3}\nu_{\rm GW}$ centred on the nominal frequency and correspondingly for the spin-down $\dot{\nu}_{\rm GW}$ consistent with previous searches (A. Ashok et al. 2021; C. J. Clark et al. 2025).

The band search is divided into multiple 10 mHz wide sub-bands and upper limits on h_0 are set in each sub-band. We obtain a mean upper limit value of h_0 across all 10 mHz bands of 1.4×10^{-26}. This is a larger than the targeted search upper limit due to the trials-factor of searching over many waveform templates. We find no evidence of gravitational wave emission in these additional extended parameter space searches as the results are consistent with Gaussian noise.

Our upper limits on h_0 can be expressed as upper limits on the ellipticity ϵ of the pulsars, modelled as a triaxial ellipsoid spinning around a principal moment of inertia axis. This is (Y. Gao et al. 2020),

$$\epsilon = 2.36 \times 10^{-6} \times \left(\frac{h_0}{10^{-25}}\right)\left(\frac{10^{45}\,\mathrm{g\,cm^2}}{I_{zz}}\right) \times \left(\frac{100\,\mathrm{Hz}}{\nu}\right)^2 \left(\frac{d}{1\,\mathrm{kpc}}\right), \quad (3)$$

where I_{zz} is the moment of inertia about the spin axis, d is the distance to the pulsar and ν is the rotational frequency. Using the canonical value of $I_{zz} = 10^{45}\,\mathrm{g\,cm^2}$ and the estimated distance using the YMW16 electron density model, gives an ellipticity upper limit of 5.5×10^{-9} and 2.1×10^{-8} at the 95 per cent confidence level for PSRs J0657−4657 and J2029−4239, respectively.

It is unlikely that our searches could have detected gravitational waves from PSRs J0657−4657 and J2029−4239, as our upper limits do not beat the spin-down lower limit $h_0^{\rm spdwn}$, assuming that all rotational energy loss is converted into gravitational waves.

4 DISCUSSION

We report results from the first MeerKAT UHF shallow survey targeting the *Fermi*-LAT sources. In this section, we evaluate the number of discoverable pulsars in both *L* band and UHF from the total discoveries and compare them to determine the most effective frequency band to find new pulsars with the MeerKAT set-up we used. We also discuss various effects that can cause difficulty finding pulsars.

4.1 Expected discoverable sources

The first full TRAPUM shallow survey was proposed as 10-min observations of 79 *Fermi*-LAT unassociated sources with four different epochs, starting with two epochs at *L* band (C. J. Clark et al. 2023). We then removed 13 sources for confirmed *L*-band discoveries to save telescope time. We added an additional 13 *Fermi*-LAT targets to match the proposed observing time for two later epochs at UHF. The UHF survey discovered nine new MSPs and six slow pulsars, while the *L*-band survey (C. J. Clark et al. 2023) found nine new MSPs and no new slow pulsars. To fairly compare the performance of the two bands, we accounted for sources that would have already been detected in one band before observations were conducted in the other, in order to avoid biasing the comparison.

For the *L*-band discoveries from C. J. Clark et al. (2023), we have the confirmation campaign where we pointed MeerKAT at these sources using the UHF receiver. All of them have been searched through the pipeline and were blindly detected at UHF. This result is also supported by a number of studies (e.g. S. D. Bates, D. R. Lorimer & J. P. W. Verbiest 2013), which shows that pulsars tend to be brighter at lower frequency (S. Johnston et al. 2020). Therefore, we conclude that all of the *L*-band pulsars are also discoverable at UHF. For the UHF discoveries, we examined nine MSPs that have also been observed at *L* band as part of the timing campaign. Of these, five sources (PSRs J1259−8148, J1356+0230, J1823+1208, J1910−5320, and J2029−4239) were not included in previous *L*-band searches, while the remaining four had been part of earlier *L*-band survey pointings but not detected. Although these earlier observations yielded no detections, we cannot rule out the possibility that the pulsars were in eclipse or otherwise obscured during those observations. Therefore, we re-evaluated their detectability using the timing observations. We used the 5-min *L*-band timing observations of these UHF discoveries for folding comparing with UHF discovery folds and 5-min UHF timing to understand S/N differences between the two bands. We then multiplied by root two (from the radiometer equation) to predict 5-min observations if they were observed for 10 min. PSRs J1259−8148, J1712−1920, J1910−5320, and J2029−4239 are clearly discoverable at *L* band as their S/Ns are above the threshold of 9 that we use in our `Peasoup` searching programme. PSR J0657−4658 is also detectable at *L* band (see Section 4.3 for more information). In contrast, PSRs J1346−2610, J1356+0230, J1823+1208, and J1831−6503 have low S/Ns of about 5–6 in the 5-min timing observations, depending on the observation day. Even after scaling to a 10-min survey observation, their S/Ns remain below our detection threshold. It is important to note that we use the known parameters from the discoveries as a starting point, and these pulsars also show signs of scintillation in frequency bands.

Therefore, we conclude that MeerKAT *L*-band observations with our search parameters and observation settings can discover

Downloaded from https://academic.oup.com/mnras/article/547/4/stag406/8501212 by guest on 05 May 2026

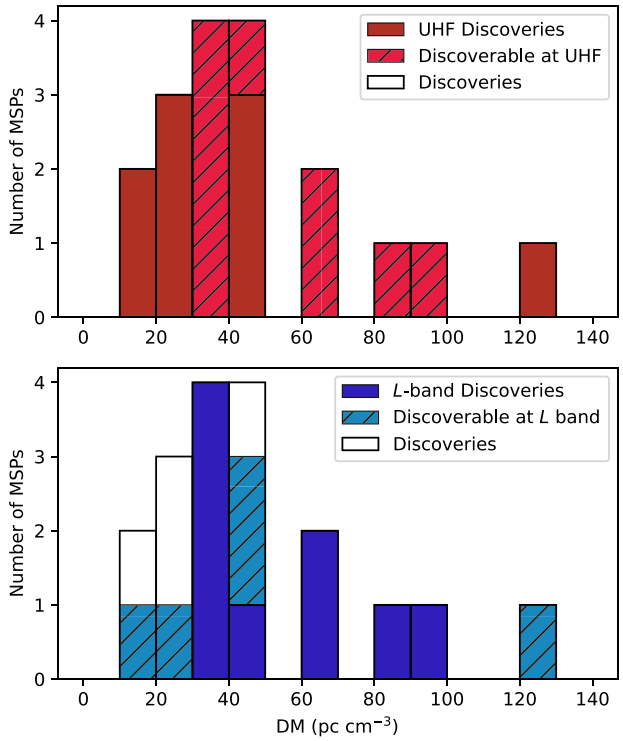

Figure 4. Histograms of discovered MSPs at *L* band (C. J. Clark et al. 2023) and UHF. The blue and red colours represent *L* band and UHF, respectively, while the red hatched histogram represents the pulsars that would have been discovered with UHF if the survey had begun at UHF instead of *L* band. This illustrates the advantage of using UHF in our set-up for discovering pulsars.

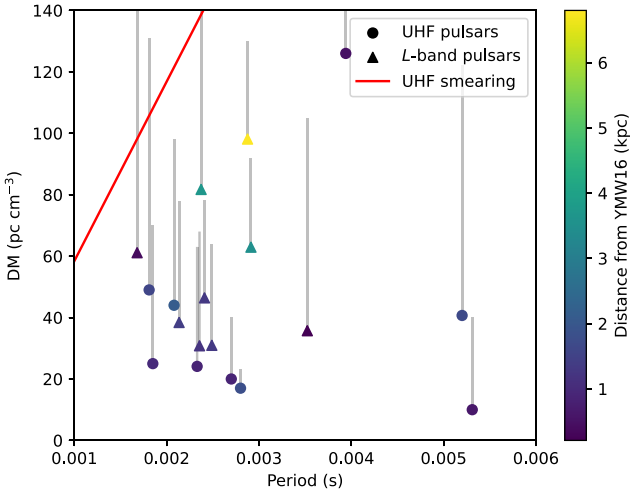

Figure 5. The distribution of discovered MSPs from the *L*-band survey (triangles; C. J. Clark et al. 2023) and the UHF survey (circles) over pulse period and DM. The colour map represents the expected distance of each MSP according to the YMW16 electron density model (J. M. Yao et al. 2017), while the grey lines display the difference between DM of each MSP and the maximum DM along the line of sight. The red line is expected discoverable pulsar periods corresponding to the DM smearing effect at UHF, while the *L*-band smearing line lies beyond the plotted range.

five UHF pulsars: PSRs J0657−4658, J1259−8148, J1712−1920, J1910−5320, and J2029−4239. The histograms of the shallow survey pulsars are shown with *L*-band pulsars, UHF pulsars, and expected discoverable sources (Fig. 4).

4.2 Comparing *L* band and UHF

We then compared the discoveries from both *L* band and UHF based on their DMs (see Fig. 4). The figure shows that many MSPs found in either band have DMs below 50 pc cm^{-3}, as our search campaign targets off-plane sources. Since these sources are located outside the Galactic plane, we anticipate lower DMs, which are consistent with expectations from electron density models such as NE2001 (J. M. Cordes & T. J. W. Lazio 2002) and YMW16 (J. M. Yao et al. 2017) along their respective lines of sight.

In terms of pulsar types, the *L*-band discoveries are all MSPs, comprising eight binaries and one isolated pulsar, with DMs ranging between 30 and 100 pc cm^{-3}; five of these pulsars fall within a narrower DM range of 30–50 pc cm^{-3}. In contrast, the UHF survey found nine MSPs and six slow pulsars. Notably, two of the UHF MSPs have DMs below 20 pc cm^{-3}, while only one, PSR J0657−4657, has a DM exceeding 100 pc cm^{-3}. Unlike the *L*-band survey, which did not detect any new slow pulsars, the UHF survey identified six, primarily via the incoherent beam. This difference is expected since the UHF incoherent beam size is approximately 50 per cent larger than that of the *L* band, allowing it to cover a larger area and thus detect slow pulsars unassociated with *Fermi* sources. After removing the slow pulsars that have been detected from the incoherent beam, there are three MSPs at low DM (lower than 30 pc cm^{-3}) that have been discovered at UHF but are not expected to be discoverable at *L* band. In addition, pulsars generally have steep spectra, making them intrinsically brighter at lower frequencies.

However, UHF has limitations, particularly due to its greater susceptibility to DM smearing. This effect, where the signal broadens and blends with noise, can make it challenging or even impossible to detect very fast-spinning pulsars, since the high time resolution required to resolve their narrow pulses is increasingly difficult to achieve at lower frequencies. The expected pulse broadening due to intra-channel DM smearing is quantified with

$$\Delta t = 4.15\ \mathrm{ms}\left(\frac{\mathrm{DM}}{\mathrm{pc\ cm^{-3}}}\right)\left[\left(\frac{\nu}{\mathrm{MHz}}\right)^{-2}-\left(\frac{\nu+\Delta\nu}{\mathrm{MHz}}\right)^{-2}\right]. \quad (4)$$

Δt is the time smearing in a single frequency channel, ν is channel centre frequency, and $\Delta\nu$ is the channel width (D. R. Lorimer & M. Kramer 2004). The pulse broadening due to DM smearing effectively sets the detection limits for pulsars in different frequency bands. Using equation (4) and assuming a 15 per cent duty cycle pulsar, we calculated the theoretical fastest discoverable pulsar, the shortest spin period detectable given the pulse broadening from DM smearing within a channel, as a function of DM for both *L* band and UHF (see Fig. 5). It is important to note that RFI conditions vary between telescope sites, some sites may experience telecommunication signals overlapping with UHF, making observations at this frequency more challenging. At the MeerKAT site, UHF actually exhibits less RFI than *L* band. However, comparing RFI fractions across different observatories is non-trivial because the measured RFI environment depends strongly on the local interference conditions, even though the number of masked channels can provide a site-specific measure.

Downloaded from https://academic.oup.com/mnras/article/547/4/stag406/8501212 by guest on 05 May 2026

4.3 Cross-matching with the *L*-band data

`Peasoup` drastically reduces the number of candidates produced by the search pipeline. Despite this, human interaction is a part of distinguishing the candidates to be either a pulsar or not. In some cases, weak signals can be seen in the resulting diagnostic plots, which is difficult to classify as a pulsar, a tier-two[17] candidate, or noise. Hence, we developed the cross-matching programme[18] to assist the candidate classification. For example, if two similar weak signals (i.e. the same candidate) show in two or more observations, there is a higher chance that the candidate is real. The cross-matching script is a PYTHON-based programme developed to check the similarity of three properties for two or more candidates from distinct observations. Those aspects are the position, the period, and the DM. For position matching, if the sky separation between two candidates is smaller than twice the assumed coherent beam FWHM, the two candidates are considered to match. However, the beam size varies with the observing angle. We use 0.007° for the beam value (∼25.2 arcsec, about the size of one coherent beam, as a rough estimation for simplification in the cross-matching script). The programme then checks the DM difference, which needs to be lower than the smearing of the full channel (*L* band at 856–1712 MHz and UHF at 544–1088 MHz) by using the DM smearing formula (D. R. Lorimer & M. Kramer 2004). Lastly, for a successful match, the two candidates must have similar spin periods. This condition is influenced by each pulsar's spin-down rate as well as Doppler shifts caused by binary motion. The spin-down rate varies from pulsar to pulsar. Typical MSP spin-down rates are below 10^{-19} ($P - \dot{P}$ diagram; D. R. Lorimer & M. Kramer 2004). We increase this to 10^{-16} to cover almost every known MSPs including those with unusually high spin-down rate. The programme calculated the change of the period by multiplying the spin-down rate and time between two epochs of an observation. Doppler shifts result from a combination of the Earth's rotation ($\sim$460 m s^{-1}), the Earth orbiting around the Sun ($\sim$30 km s^{-1}), and a pulsar orbiting within its binary system ($\sim$300 km s^{-1}). We selected large values for each parameter to get loosely constrained results by the notion that getting a higher number of matches is better than missing potential matches. With the three conditions are satisfied, the programme flags the candidates as a potential match. We then carry out final confirmation manually. We applied this programme to data from two *L*-band epochs (C. J. Clark et al. 2023) and two UHF epochs. However, some targets had only two or three usable epochs due to corrupted files from cluster downtimes. The programme identified 85 pairs of candidates, though we cannot estimate the total number of potentially missed pairs due to incomplete or corrupted input data. Upon reviewing the results, we found some pairs represented genuine discoveries, either matches within *L*-band or UHF data, while others were RFI. The results demonstrated that the programme could reliably identify plausible candidate matches.

We identified a weak pulsar candidate associated with 4FGL J0657.4−4658 from the *L*-band survey (C. J. Clark et al. 2023). This candidate had a S/N of approximately ∼11 at *L* band, compared to a higher S/N of ∼19 at UHF. The *L*-band detection may be classified as a tier-two candidate, as it is relatively faint and affected by smearing, warranting follow-up observations for confirmation. Using our cross-matching script, we found that this *L*-band candidate corresponded to one of the UHF discoveries, confirming it as a real pulsar and demonstrating the effectiveness of the cross-matching method.

[17]We define tier-two candidates as ambiguous detections, such as those with signal-to-noise ratios close to our threshold of 9, or candidates whose pulse profiles are comparable in width to the expected DM smearing, making classification more difficult.
[18]https://github.com/01tinn/cross_matching

5 CONCLUSIONS AND FUTURE WORK

The paper described the first UHF shallow (10 min) survey of 79 unassociated *Fermi* gamma-ray sources with MeerKAT. Using MeerKAT beam forming, up to 480 coherent beams were formed to cover the *Fermi* localization region for each target.

We found 15 new pulsars. Seven of them are MSPs associated with *Fermi*-LAT gamma-ray sources, two additional MSPs are candidate associations that require confirmation from gamma-ray pulsations, and six slow pulsars not associated with *Fermi*-LAT sources. Among the nine MSPs, eight are in binary systems and one new MSP (PSR J2029-4239) is an isolated pulsar. Further investigation indicated that PSRs J1346−2610, J1712−1920, and J1910−5320 are RBs; PSRs J1259−8148, J1356+0230, and J1831−6503 are BWs due to their orbital periods, companion masses, and eclipses. Two other systems (PSRs J0657−4657 and J1823+1208) are He white dwarf binaries.

For future work, we have started the expanded UHF shallow survey targeting 145 *Fermi*-LAT sources that have generally not been previously observed from the latest 4FGL-DR4 catalogue (J. Ballet et al. 2023). The upcoming *Fermi*-LAT catalogue will provide improved source localizations for future targeted radio pulsar searches. The UHF survey presented in this paper is part of a larger programme that also includes *L*-band observations (C. J. Clark et al. 2023), this new survey is conducted exclusively at UHF, as our results show that UHF with our observing parameters is more effective than *L* band for finding pulsars. At the time of writing this paper, we found 23 new pulsars from the expanded UHF survey (Thongmeearkom et al., in preparation).

ACKNOWLEDGEMENTS

The MeerKAT telescope is operated by the South African Radio Astronomy Observatory (SARAO), which is a facility of the National Research Foundation, an agency of the Department of Science and Innovation. We thank staff at SARAO for their help with observations and commissioning. TRAPUM observations used the FBFUSE and APSUSE computing clusters for data acquisition, storage and analysis. These clusters were funded and installed by the Max-Planck-Institut für Radioastronomie (MPIfR) and the Max-Planck-Gesellschaft. The National Radio Astronomy Observatory is a facility of the National Science Foundation operated under cooperative agreement by Associated Universities, Inc. The Parkes radio telescope is part of the Australia Telescope National Facility (https://ror.org/05qajvd42) which is funded by the Australian Government for operation as a National Facility managed by CSIRO. We acknowledge the Wiradjuri people as the traditional owners of the Observatory site. The Nançay Radio Observatory is operated by the Paris Observatory, associated with the French Centre National de la Recherche Scientifique (CNRS) and Université d'Orléans. It is partially supported by the Region Centre Val de Loire in France.

The *Fermi* LAT Collaboration acknowledges generous ongoing support from a number of agencies and institutes that have supported both the development and the operation of the LAT

Downloaded from https://academic.oup.com/mnras/article/547/4/stag406/8501212 by guest on 05 May 2026

as well as scientific data analysis. These include the National Aeronautics and Space Administration and the Department of Energy in the United States, the Commissariat à l'Energie Atomique and the Centre National de la Recherche Scientifique / Institut National de Physique Nucléaire et de Physique des Particules in France, the Agenzia Spaziale Italiana and the Istituto Nazionale di Fisica Nucleare in Italy, the Ministry of Education, Culture, Sports, Science and Technology (MEXT), High Energy Accelerator Research Organization (KEK) and Japan Aerospace Exploration Agency (JAXA) in Japan, and the K. A. Wallenberg Foundation, the Swedish Research Council and the Swedish National Space Board in Sweden.

Additional support for science analysis during the operations phase is gratefully acknowledged from the Istituto Nazionale di Astrofisica in Italy and the Centre National d'Études Spatiales in France. This work performed in part under DOE Contract DE-AC02-76SF00515.

This research has made use of data or software obtained from the Gravitational Wave Open Science Center (gwosc.org), a service of the LIGO Scientific Collaboration, the Virgo Collaboration, and KAGRA. This material is based upon work supported by NSF's LIGO Laboratory which is a major facility fully funded by the National Science Foundation, as well as the Science and Technology Facilities Council (STFC) of the United Kingdom, the Max-Planck-Society (MPS), and the State of Niedersachsen/Germany for support of the construction of Advanced LIGO and construction and operation of the GEO600 detector. Additional support for Advanced LIGO was provided by the Australian Research Council.

This manuscript is based on material presented in the first author's doctoral thesis (T. Thongmeearkom 2025), which was written in journal format and contains an earlier draft of this paper. Parts of the text have been revised and expanded for publication.

TT is grateful to the National Astronomical Research Institute of Thailand (NARIT) for awarding a student scholarship. MB acknowledges resources from the research grant 'iPeska' (PI: Andrea Possenti), funded under the INAF national call Prin-SKA/CTA approved with the Presidential Decree 70/2016. JB is supported by the National Aeronautics and Space Administration (NASA) under award number 80GSFC21M0002. ECF is supported by the National Aeronautics and Space Administration (NASA) under award number 80GSFC24M0006. LV acknowledges financial support from the Dean's Doctoral Scholar Award from the University of Manchester and partial support from the National Science Foundation (NSF) grant AST-1816492. SBD acknowledges the support from the Science and Technology Facilities Council (STFC) (grant number: ST/X001229/1) to permit work as a postgraduate researcher. VSD and ULTRACAM are supported by the Science and Technology Facilities Council (STFC) grant ST/Z000033/1.

We thank Matthew Kerr for reviewing this manuscript on behalf of the *Fermi*-LAT collaboration. We are grateful to the scientific editor, Timothy J. Pearson, for helpful suggestions and to the referee, David A. Smith, for valuable comments.

DATA AVAILABILITY

TRAPUM data products are available upon reasonable request to the TRAPUM collaboration. The *Fermi*-LAT data are available from the *Fermi* Science Support Center (http://fermi.gsfc.nasa.gov/ssc).

REFERENCES

Abbott R. et al., 2021, SoftwareX, 13, 100658
Abbott R. et al., 2023, ApJS, 267, 29
Abdollahi S. et al., 2020, ApJS, 247, 33
Abdollahi S. et al., 2022, ApJS, 260, 53
Acero F. et al., 2016, ApJS, 223, 26
Ackermann M. et al., 2012, ApJ, 753, 83
Ashok A. et al., 2021, ApJ, 923, 85
Atwood W. B. et al., 2009, ApJ, 697, 1071
Atwood W. et al., 2013, in Brandt T. J., Omodei N., Wilson-Hodge C., eds, Fermi Symposium Proceedings - eConf C121028, 4th International Fermi Symposium. Monterey, USA, p. 8
Au K.-Y. et al., 2023, ApJ, 943, 103
Bailes M. et al., 2020, Publ. Astron. Soc. Aust., 37, e028
Ballet J., Bruel P., Burnett T. H., Lott B., The Fermi-LAT collaboration, 2023, preprint (arXiv:2307.12546)
Bangale P. et al., 2024, ApJ, 966, 161
Barr E. D., 2018, in Weltevrede P., Perera B. B. P., Preston L. L., Sanidas S., eds, Proc. IAU Symp. Vol. 337, Pulsar Astrophysics the Next Fifty Years, An S-band Receiver and Backend System for MeerKAT. Cambridge Univ. Press, Cambridge, p. 175
Barr E., 2020, Astrophysics Source Code Library, record ascl:2001.014
Bates S. D., Lorimer D. R., Verbiest J. P. W., 2013, MNRAS, 431, 1352
Belmonte Díaz S. et al., 2025, MNRAS, 543, 3019
Benvenuto O. G., De Vito M. A., Horvath J. E., 2014, ApJ, 786, L7
Bezuidenhout M. C. et al., 2023, RAS Techn. Instr., 2, 114
Bickel P., Kleijn B., Rice J., 2008, ApJ, 685, 384
Booth R. S., de Blok W. J. G., Jonas J. L., Fanaroff B., 2009, preprint (arXiv:0910.2935)
Breton R. P., Roberts M. S. E., Ransom S. M., Kaspi V. M., Durant M., Bergeron P., Faulkner A. J., 2007, ApJ, 661, 1073
Breton R. P., Rappaport S. A., van Kerkwijk M. H., Carter J. A., 2012, ApJ, 748, 115
Breton R. P. et al., 2013, ApJ, 769, 108
Brown A. J. et al., 2022, MNRAS, 513, 3050
Bruel P., 2019, A&A, 622, A108
Bruel P., Burnett T. H., Digel S. W., Johannesson G., Omodei N., Wood M., 2018, preprint (arXiv:1810.11394)
Burgay M. et al., 2024, A&A, 691, A315
Callanan P. J., van Paradijs J., Rengelink R., 1995, ApJ, 439, 928
Camilo F. et al., 2015, ApJ, 810, 85
Carli E. et al., 2024, MNRAS, 531, 2835
Chambers K. C. et al., 2016, preprint (arXiv:1612.05560)
Chen H.-L., Chen X., Tauris T. M., Han Z., 2013, ApJ, 775, 27
Chen W., Barr E., Karuppusamy R., Kramer M., Stappers B., 2021, J. Astron. Instr., 10, 2150013
Clark C. J. et al., 2023, MNRAS, 519, 5590
Clark C. J. et al., 2025, ApJ, 994, 149
Clark C. J., Valtolina S., Nieder L., van Haasteren R., 2026, preprint (arXiv:2601.07592)
Clemens J. C., Crain J. A., Anderson R., 2004, in Moorwood A. F. M., Iye M., eds, Proc. SPIE Conf. Ser. Vol. 5492, Ground-based Instrumentation for Astronomy. SPIE, Bellingham, p. 331
Cordes J. M., Lazio T. J. W., 2002, preprint (astro-ph/0207156)
Cromartie H. T. et al., 2016, ApJ, 819, 34
Cutler C., Schutz B. F., 2005, Phys. Rev. D, 72, 063006
Damour T., Taylor J. H., 1991, ApJ, 366, 501
de Jager O. C., Raubenheimer B. C., Swanepoel J. W. H., 1989, A&A, 221, 180
Deneva J. S. et al., 2016, ApJ, 823, 105
Dhillon V. S. et al., 2007, MNRAS, 378, 825
Dhillon V. S. et al., 2021, MNRAS, 507, 350
Djorgovski S. G. et al., 2011, preprint (arXiv:1102.5004)
Dodge O. G. et al., 2024, MNRAS, 528, 4337
Finke T., Krämer M., Manconi S., 2021, MNRAS, 507, 4061
Flewelling H. A. et al., 2020, ApJS, 251, 7

Downloaded from https://academic.oup.com/mnras/article/547/4/stag406/8501212 by guest on 05 May 2026

Foreman-Mackey D., Hogg D. W., Lang D., Goodman J., 2013, PASP, 125, 306
Freire P. C. C., Ridolfi A., 2018, MNRAS, 476, 4794
Gao Y., Shao L., Xu R., Sun L., Liu C., Xu R.-X., 2020, MNRAS, 498, 1826
Ghosh A. et al., 2024, ApJ, 965, 64
Haslam C. G. T., Salter C. J., Stoffel H., Wilson W. E., 1982, A&AS, 47, 1
Hobbs G. B., Edwards R. T., Manchester R. N., 2006, MNRAS, 369, 655
Hobbs G. et al., 2020, PASA, 37, e012
Jankowski F., van Straten W., Keane E. F., Bailes M., Barr E. D., Johnston S., Kerr M., 2018, MNRAS, 473, 4436
Jaranowski P., Królak A., Schutz B. F., 1998, Phys. Rev. D, 58, 063001
Johnston S. et al., 2020, MNRAS, 493, 3608
Jonas J., MeerKAT Team, 2016, Proc. Sci., MeerKAT Science: On the Pathway to the SKA. SISSA, Trieste, PoS#1
Jones D. I., 2015, MNRAS, 453, 53
Keith M. J. et al., 2011, MNRAS, 414, 1292
Kerr M., 2011, ApJ, 732, 38
Kerr M. et al., 2012, ApJ, 748, L2
Kerr M. et al., 2025, ApJ, 984, 180
Koljonen K. I. I., Linares M., 2025, ApJ, 994, 8
Lee K. J., Guillemot L., Yue Y. L., Kramer M., Champion D. J., 2012, MNRAS, 424, 2832
Lorimer D. R., Kramer M., 2004, Handbook of Pulsar Astronomy, Vol. 4. Cambridge Univ. Press, Cambridge
Luo S., Leung A. P., Hui C. Y., Li K. L., 2020, MNRAS, 492, 5377
Luo J. et al., 2021, ApJ, 911, 45
Mata Sánchez D., Istrate A. G., van Kerkwijk M. H., Breton R. P., Kaplan D. L., 2020, MNRAS, 494, 4031
Men Y., Barr E., Clark C. J., Carli E., Desvignes G., 2023, A&A, 679, A20
Morello V. et al., 2019, MNRAS, 483, 3673
Nieder L. et al., 2019, ApJ, 883, 42
Nieder L., Allen B., Clark C. J., Pletsch H. J., 2020a, ApJ, 901, 156
Nieder L. et al., 2020b, ApJ, 902, L46
Obrocka M., Stappers B., Wilkinson P., 2015, A&A, 579, A69
Padmanabh P. V. et al., 2023, MNRAS, 524, 1291
Perez K. I., Bogdanov S., Halpern J. P., Gajjar V., 2023, ApJ, 952, 150
Pletsch H. J., Clark C. J., 2014, ApJ, 795, 75
Polzin E. J. et al., 2018, MNRAS, 476, 1968
Polzin E. J., Breton R. P., Stappers B. W., Bhattacharyya B., Janssen G. H., Osłowski S., Roberts M. S. E., Sobey C., 2019, MNRAS, 490, 889
Polzin E. J., Breton R. P., Bhattacharyya B., Scholte D., Sobey C., Stappers B. W., 2020, MNRAS, 494, 2948
Prayag V. et al., 2024, MNRAS, 533, 2570
Purcell C. R. et al., 2015, ApJ, 804, 22
Ransom S., 2011, Astrophysics Source Code Library, record ascl:1107.017
Ransom S. M. et al., 2011, ApJ, 727, L16
Ray P. S. et al., 2012, preprint (arXiv:1205.3089)
Ray P. S. et al., 2022, ApJ, 927, 216
Remazeilles M., Dickinson C., Banday A. J., Bigot-Sazy M. A., Ghosh T., 2015, MNRAS, 451, 4311
Ridolfi A. et al., 2021, MNRAS, 504, 1407
Roberts M. S. E., 2012, Proc. Int. Astron. Un., 8, 127
Saz Parkinson P. M., Xu H., Yu P. L. H., Salvetti D., Marelli M., Falcone A. D., 2016, ApJ, 820, 8
Shang L. et al., 2024, ApJ, 969, 62
Shklovskii I. S., 1970, Sov. Ast., 13, 562
Simpson J. A., Linares M., Casares J., Shahbaz T., Sen B., Camilo F., 2025, MNRAS, 536, 2169
Smith D. A. et al., 2019, ApJ, 871, 78
Smith D. A. et al., 2023, ApJ, 958, 191
Stappers B., Kramer M., 2018, Proc. Sci. Vol. 277, An Update on TRAPUM. SISSA, Trieste, PoS(MeerKAT2016)009
Strader J. et al., 2019, ApJ, 872, 42
Strader J. et al., 2025, ApJ, 980, 124
Swihart S. J., Strader J., Chomiuk L., Aydi E., Sokolovsky K. V., Ray P. S., Kerr M., 2022, ApJ, 941, 199
Tauris T. M., van den Heuvel E. P. J., 2023, Physics of Binary Star Evolution. From Stars to X-ray Binaries and Gravitational Wave Sources. Princeton Univ. Press, Princeton
The LIGO Scientific Collaboration, 2025, preprint (arXiv:2508.18079)
Thongmeearkom T., 2021, MPhil thesis, The University of Manchester
Thongmeearkom T., 2025, PhD thesis, The University of Manchester
Thongmeearkom T. et al., 2024, MNRAS, 530, 4676
Tian J. et al., 2025, MNRAS, 544, 1843
Turner J. D. et al., 2024, MNRAS, 531, 3579
Vleeschower L. et al., 2024, MNRAS, 530, 1436
Wang P. et al., 2021, Sci. China Phys. Mech. Astron., 64, 129562
Yao J. M., Manchester R. N., Wang N., 2017, ApJ, 835, 29
Zhu W. W. et al., 2014, ApJ, 781, 117

SUPPORTING INFORMATION

Supplementary data are available at *MNRAS* online.

J0657-4657.par
J1207-45.par
J1259-8148.par
J1303-4713.par
J1346-2610.par
J1356+0230.par
J1712-1920.par
J1816-64.par
J1823+1208.par
J1831-6503.par
J1845-25.par
J1924-10.par
J2029-4239.par
J2355-66.par
UHF_OBS_epoch1.csv
UHF_OBS_epoch2.csv

Please note: Oxford University Press is not responsible for the content or functionality of any supporting materials supplied by the authors. Any queries (other than missing material) should be directed to the corresponding author for the article.

APPENDIX A: OBSERVATIONS AND SLOW PULSARS

Tables A1 and A2 summarize the UHF observations of *Fermi*-LAT sources, while Table A3 presents initial information on the slow pulsars discussed in this work. The observational tables and the timing parameter (.par) files corresponding to the slow pulsars are available as supplementary material accompanying this paper.

Downloaded from https://academic.oup.com/mnras/article/547/4/stag406/8501212 by guest on 05 May 2026

Table A1. A list of UHF survey observations of *Fermi*-LAT sources for the first epoch. $S_{\rm min}$, $S_{\rm med}$, and S_{95} are sensitivity estimates from the radiometer equation. $S_{\rm min}$ represents a pulsar located at the centre of a coherent beam under ideal assumptions, while $S_{\rm med}$ (median) and S_{95} (95th percentile) account for the tiling pattern of the beams. nAnt is the number of antennas. $T_{\rm sky}$ and $T_{\rm sys}$ are the sky and system temperatures, respectively. Pulsars discovered in this survey (including both confirmed and unconfirmed *Fermi*-LAT associations) are indicated with an asterisk (∗), while those from other *Fermi*-TRAPUM surveys are marked with a dagger (†).

4FGL NAME	R.A. (J2000)	Decl. (J2000)	MJD	$S_{\rm min}$ (μJy)	$S_{\rm med}$ (μJy)	S_{95} (μJy)	nAnt	$T_{\rm sky}$ (K)	$T_{\rm sys}$ (K)
J0048.6−6347	$00^{\rm h}48^{\rm m}40\overset{\rm s}{.}44$	−63°47′29.″0433	59471.7393	69	148	167	56	3.9	22.4
J0139.5−2228	$01^{\rm h}39^{\rm m}35\overset{\rm s}{.}3041$	−22°28′39.″7174	59471.8307	68	153	183	56	3.4	21.9
J0414.7−4300	$04^{\rm h}14^{\rm m}47\overset{\rm s}{.}4481$	−43°00′43.″2037	59563.0916	62	106	122	60	2.6	21.1
J0529.9−0224	$05^{\rm h}29^{\rm m}54\overset{\rm s}{.}4794$	−02°24′17.″2798	59563.0843	69	121	137	60	4.8	23.3
J0540.0−7552	$05^{\rm h}40^{\rm m}01\overset{\rm s}{.}5363$	−75°52′41.″5082	59563.1874	64	96	115	60	3.1	21.6
J0657.4−4658∗	$06^{\rm h}57^{\rm m}26\overset{\rm s}{.}3525$	−46°58′48.″7262	59716.3578	76	111	130	56	3.4	22.0
J0712.0−6431	$07^{\rm h}12^{\rm m}01\overset{\rm s}{.}9208$	−64°31′32.″1478	59730.3127	64	115	133	60	3.0	21.5
J0906.8−2122	$09^{\rm h}06^{\rm m}49\overset{\rm s}{.}1052$	−21°22′20.″641	59496.4563	63	118	133	60	2.6	21.2
J0953.6−1509	$09^{\rm h}53^{\rm m}37\overset{\rm s}{.}3206$	−15°09′17.″6385	59496.4402	64	81	93	60	3.1	21.7
J1036.6−4349	$10^{\rm h}36^{\rm m}36\overset{\rm s}{.}167$	−43°49′26.″0339	59496.5378	68	98	116	60	4.2	22.7
J1106.7−1742	$11^{\rm h}06^{\rm m}47\overset{\rm s}{.}7612$	−17°42′53.″2796	59496.5302	64	91	106	60	3.2	21.7
J1120.0−2204	$11^{\rm h}20^{\rm m}00\overset{\rm s}{.}3845$	−22°04′40.″4398	59563.1075	62	74	82	60	2.5	21.1
J1126.0−5007	$11^{\rm h}26^{\rm m}03\overset{\rm s}{.}479$	−50°07′09.″8401	59496.5449	69	116	134	60	4.3	22.8
J1204.5−5032	$12^{\rm h}04^{\rm m}35\overset{\rm s}{.}592$	−50°32′44.″1632	59887.1282	67	126	144	60	4.8	23.3
J1207.4−4536∗	$12^{\rm h}07^{\rm m}29\overset{\rm s}{.}6155$	−45°36′44.″9973	59563.0618	66	115	131	60	3.6	22.2
J1213.9−4416†	$12^{\rm h}13^{\rm m}58\overset{\rm s}{.}656$	−44°16′46.″1966	59563.0688	66	98	115	60	3.7	22.2
J1259.0−8148∗	$12^{\rm h}59^{\rm m}02\overset{\rm s}{.}9993$	−81°48′58.″678	59471.7322	70	156	182	56	3.9	22.5
J1303.1−4714∗	$13^{\rm h}03^{\rm m}09\overset{\rm s}{.}071$	−47°14′17.″1533	59471.718	77	172	201	56	5.3	23.9
J1345.9−2612∗	$13^{\rm h}45^{\rm m}55\overset{\rm s}{.}5615$	−26°12′41.″7577	59563.1001	69	112	130	60	4.7	23.2
J1356.6+0234∗	$13^{\rm h}56^{\rm m}39\overset{\rm s}{.}3347$	+02°34′38.″2803	59563.1296	65	119	132	60	3.4	21.9
J1400.0−2415	$14^{\rm h}00^{\rm m}04\overset{\rm s}{.}9438$	−24°15′57.″6027	59563.1223	69	101	119	60	4.6	23.2
J1416.7−5023	$14^{\rm h}16^{\rm m}42\overset{\rm s}{.}7441$	−50°23′22.″1988	59563.076	83	121	141	60	9.8	28.4
J1450.8−1424	$14^{\rm h}50^{\rm m}50\overset{\rm s}{.}592$	−14°24′21.″24	59563.1368	69	117	135	60	4.9	23.4
J1458.8−2120	$14^{\rm h}58^{\rm m}48\overset{\rm s}{.}7903$	−21°20′19.″6815	59563.1726	71	100	117	60	5.6	24.1
J1513.7−1519	$15^{\rm h}13^{\rm m}46\overset{\rm s}{.}6809$	−15°19′59.″1611	59563.1512	73	105	123	60	6.3	24.8
J1517.7−4446	$15^{\rm h}17^{\rm m}42\overset{\rm s}{.}7185$	−44°46′36.″1166	59563.115	90	156	177	60	12.2	30.8
J1526.6−3810	$15^{\rm h}26^{\rm m}38\overset{\rm s}{.}2544$	−38°10′08.″3954	59563.1439	87	154	172	60	11.0	29.5
J1527.8+1013	$15^{\rm h}27^{\rm m}53\overset{\rm s}{.}0164$	+10°13′42.″9584	59496.4178	72	138	157	60	6.0	24.5
J1530.0−1522	$15^{\rm h}30^{\rm m}00\overset{\rm s}{.}2637$	−15°22′33.″241	59563.18	74	137	153	60	6.4	24.9
J1539.4−3323	$15^{\rm h}39^{\rm m}24\overset{\rm s}{.}2651$	−33°23′55.″3226	59563.1654	79	89	96	60	8.4	27.0
J1543.6−0244	$15^{\rm h}43^{\rm m}37\overset{\rm s}{.}8479$	−02°44′49.″5604	59471.7711	72	157	180	56	4.5	23.0
J1544.2−2554†	$15^{\rm h}44^{\rm m}12\overset{\rm s}{.}5537$	−25°54′45.″0014	59563.1583	75	95	109	60	6.9	25.5
J1612.1+1407	$16^{\rm h}12^{\rm m}07\overset{\rm s}{.}511$	+14°07′00.″4811	59496.4787	81	121	142	60	8.5	27.0
J1622.2−7202	$16^{\rm h}22^{\rm m}12\overset{\rm s}{.}6013$	−72°02′23.″6462	59471.7859	75	162	185	56	5.5	24.0
J1630.1−1049	$16^{\rm h}30^{\rm m}06\overset{\rm s}{.}936$	−10°49′05.″8809	59496.4043	83	122	143	60	7.0	25.5
J1641.3−2908	$16^{\rm h}41^{\rm m}21\overset{\rm s}{.}3611$	−29°08′21.″4778	59471.8387	91	206	245	56	10.6	29.1
J1646.7−2154	$16^{\rm h}46^{\rm m}44\overset{\rm s}{.}425$	−21°54′26.″9975	59471.8225	89	202	243	56	10.1	28.6
J1656.4−0410	$16^{\rm h}56^{\rm m}28\overset{\rm s}{.}656$	−04°10′12.″7195	59496.4484	76	111	131	60	6.8	25.4
J1659.0−0140	$16^{\rm h}59^{\rm m}03\overset{\rm s}{.}7207$	−01°40′39″	59496.5004	79	115	134	60	8.2	26.8
J1708.8−0923	$17^{\rm h}08^{\rm m}48\overset{\rm s}{.}0981$	−09°23′39.″4817	59496.4253	81	160	185	60	8.4	27.0
J1709.4−2127	$17^{\rm h}09^{\rm m}25\overset{\rm s}{.}3711$	−21°27′23.″0397	59496.4108	95	168	191	60	12.6	31.1
J1709.9−0900	$17^{\rm h}09^{\rm m}56\overset{\rm s}{.}0156$	−09°00′51.″8383	59496.4325	82	161	185	60	8.4	26.9
J1711.9−1922∗	$17^{\rm h}11^{\rm m}54\overset{\rm s}{.}624$	−19°22′03.″3582	59496.4934	88	124	146	60	10.7	29.3
J1717.5−5804	$17^{\rm h}17^{\rm m}30\overset{\rm s}{.}813$	−58°04′14.″155	59471.7932	92	200	228	56	10.8	29.4
J1720.6+0708	$17^{\rm h}20^{\rm m}39\overset{\rm s}{.}3091$	+07°08′48.″8406	59471.8153	90	196	227	56	10.2	28.7
J1722.8−0418	$17^{\rm h}22^{\rm m}50\overset{\rm s}{.}7568$	−04°18′11.″8797	59496.4718	84	110	128	60	8.8	27.3
J1727.4+0326	$17^{\rm h}27^{\rm m}27\overset{\rm s}{.}1436$	+03°26′59.″2801	59496.4644	82	115	135	60	8.7	27.2
J1730.4−0359	$17^{\rm h}30^{\rm m}26\overset{\rm s}{.}0669$	−03°59′32.″2801	59471.7782	88	182	207	56	9.8	28.3
J1735.3−0717	$17^{\rm h}35^{\rm m}21\overset{\rm s}{.}6211$	−07°17′07.″0792	59471.8549	95	211	248	56	11.5	30.1
J1739.1−1059	$17^{\rm h}39^{\rm m}08\overset{\rm s}{.}064$	−10°59′41.″2786	59471.862	99	230	286	56	12.9	31.5
J1747.6+0324	$17^{\rm h}47^{\rm m}37\overset{\rm s}{.}2217$	+03°24′26.″28	59496.5152	90	125	147	60	11.3	29.9
J1749.8−0303	$17^{\rm h}49^{\rm m}50\overset{\rm s}{.}9253$	−03°03′06.″48	59496.4863	96	137	162	60	12.9	31.4
J1813.7−6846	$18^{\rm h}13^{\rm m}47\overset{\rm s}{.}5415$	−68°46′42.″6123	59786.0961	70	98	117	60	5.8	24.3
J1816.4−6405∗	$18^{\rm h}16^{\rm m}27\overset{\rm s}{.}5977$	−64°05′05.″9967	59786.089	73	95	111	60	7.0	25.5
J1816.7+1749	$18^{\rm h}16^{\rm m}45\overset{\rm s}{.}0513$	+17°49′40.″4398	59471.8081	86	187	213	56	9.0	27.6
J1818.6+1316	$18^{\rm h}18^{\rm m}36\overset{\rm s}{.}6504$	+13°16′23.″1596	59471.7475	86	188	214	56	9.2	27.8
J1822.9−4718	$18^{\rm h}22^{\rm m}56\overset{\rm s}{.}6895$	−47°18′16.″9162	59786.0742	76	96	111	60	8.0	26.6
J1823.2+1209∗	$18^{\rm h}23^{\rm m}14\overset{\rm s}{.}8828$	+12°09′26.″28	59471.8475	90	205	246	56	10.5	29.0
J1824.2−5427	$18^{\rm h}24^{\rm m}16\overset{\rm s}{.}897$	−54°27′05.″0427	59471.8003	77	166	188	56	6.2	24.7
J1827.5+1141	$18^{\rm h}27^{\rm m}30\overset{\rm s}{.}8643$	+11°41′10.″681	59471.7546	94	201	228	56	11.3	29.9

Downloaded from https://academic.oup.com/mnras/article/547/4/stag406/8501212 by guest on 05 May 2026

Table A1 – *continued*

4FGL NAME	R.A. (J2000)	Decl. (J2000)	MJD	S_{min} (μJy)	S_{med} (μJy)	S_{95} (μJy)	nAnt	T_{sky} (K)	T_{sys} (K)
J1831.1−6503∗	$18^h31^m06^s.5552$	−65°03′57″.2498	59786.1032	71	81	90	60	6.2	24.8
J1845.8−2521∗	$18^h45^m51^s.5552$	−25°21′30″.5983	59786.067	90	116	134	60	13.0	31.5
J1906.0−1718	$19^h06^m04^s.4604$	−17°18′55″.08	59786.0523	81	127	147	60	9.7	28.3
J1910.7−5320∗	$19^h10^m47^s.7393$	−53°20′18″.6035	59716.312	85	137	159	56	5.8	24.3
J1913.4−1526	$19^h13^m24^s.3604$	−15°26′58″.5608	59496.508	85	123	145	60	9.5	28.1
J1916.8−3025	$19^h16^m53^s.6865$	−30°25′28″.5622	59835.7782	83	98	109	56	8.2	26.8
J1924.8−1035∗	$19^h24^m49^s.27$	−10°35′27″.2415	59786.0301	83	100	112	60	10.2	28.8
J1947.6−1121	$19^h47^m39^s.8657$	−11°21′54″.7202	59786.0816	73	96	110	60	6.8	25.4
J2026.3+1431	$20^h26^m23^s.7085$	+14°31′21″.0001	59786.0596	68	88	101	60	5.2	23.7
J2029.5−4237∗	$20^h29^m30^s.3589$	−42°37′42″.6068	59496.5226	73	140	162	60	5.7	24.2
J2043.9−4802	$20^h43^m55^s.5615$	−48°02′23″.2755	59786.0375	67	86	98	60	5.0	23.5
J2112.5−3043	$21^h12^m33^s.6035$	−30°43′45″.4784	59786.0448	66	71	75	60	4.4	23.0
J2121.8−3412	$21^h21^m53^s.811$	−34°12′11″.8817	59730.297	70	140	163	60	4.1	22.6
J2133.1−6432	$21^h33^m10^s.8252$	−64°32′17″.8784	59786.1105	65	83	95	60	4.2	22.8
J2201.0−6928	$22^h01^m01^s.6772$	−69°28′26″.0394	59730.3039	70	109	130	60	4.2	22.7
J2212.4+0708	$22^h12^m25^s.9937$	+07°08′34″.0795	59730.2817	70	106	129	60	3.8	22.3
J2219.7−6837	$22^h19^m47^s.2559$	−68°37′02″.287	59730.2893	71	101	120	60	3.9	22.4
J2241.4−8327	$22^h41^m25^s.6348$	−83°27′40″.3088	59471.7251	72	158	183	56	4.2	22.7
J2355.5−6614∗	$23^h55^m33^s.7939$	−66°14′04″.1895	59471.7627	71	159	187	56	3.9	22.4

Table A2. A list of UHF survey observations of *Fermi*-LAT sources for the second epoch. S_{min}, S_{med}, and S_{95} are sensitivity estimates from the radiometer equation. S_{min} represents a pulsar located at the centre of a coherent beam under ideal assumptions, while S_{med} (median) and S_{95} (95th percentile) account for the tiling pattern of the beams. nAnt is the number of antennas. T_{sky} and T_{sys} are the sky and system temperatures, respectively. Pulsars discovered in this survey (including both confirmed and unconfirmed *Fermi*-LAT associations) are indicated with an asterisk (∗), while those from other *Fermi*-TRAPUM surveys are marked with a dagger (†). Dashes (–) indicate missing values corresponding to sources removed from the second epoch after being independently discovered by other surveys.

4FGL NAME	R.A. (J2000)	Decl. (J2000)	MJD	S_{min} (μJy)	S_{med} (μJy)	S_{95} (μJy)	nAnt	T_{sky} (K)	T_{sys} (K)
J0048.6−6347	$00^h48^m40^s.44$	−63°47′29″.0433	59882.0926	64	91	108	60	3.9	22.4
J0139.5−2228	$01^h39^m35^s.3041$	−22°28′39″.7174	59882.0854	64	109	124	60	3.4	21.9
J0414.7−4300	$04^h14^m47^s.4481$	−43°00′43″.2037	59887.1587	61	120	135	60	2.6	21.1
J0529.9−0224	$05^h29^m54^s.4794$	−02°24′17″.2798	59887.1435	67	136	151	60	4.8	23.3
J0540.0−7552	$05^h40^m01^s.5363$	−75°52′41″.5082	59887.1512	62	105	125	60	3.1	21.6
J0657.4−4658∗	$06^h57^m26^s.3525$	−46°58′48″.7262	59730.3197	68	111	132	60	3.4	22.0
J0712.0−6431	$07^h12^m01^s.9208$	−64°31′32″.1478	59786.1495	62	91	107	60	3.0	21.5
J0906.8−2122	$09^h06^m49^s.1052$	−21°22′20″.641	59978.1197	61	112	128	60	2.6	21.2
J0953.6−1509	$09^h53^m37^s.3206$	−15°09′17″.6385	59887.1066	62	81	94	60	3.1	21.7
J1036.6−4349	$10^h36^m36^s.167$	−43°49′26″.0339	–	–	–	–	–	–	–
J1106.7−1742	$11^h06^m47^s.7612$	−17°42′53″.2796	59887.0924	63	93	110	60	3.2	21.7
J1120.0−2204	$11^h20^m00^s.3845$	−22°04′40″.4398	59887.0994	60	67	72	60	2.5	21.1
J1126.0−5007	$11^h26^m03^s.479$	−50°07′09″.8401	59886.0715	71	108	124	56	4.3	22.8
J1204.5−5032	$12^h04^m35^s.592$	−50°32′44″.1632	–	–	–	–	–	–	–
J1207.4−4536∗	$12^h07^m29^s.6155$	−45°36′44″.9973	59887.121	63	107	127	60	3.6	22.2
J1213.9−4416†	$12^h13^m58^s.656$	−44°16′46″.1966	59887.114	64	87	103	60	3.7	22.2
J1259.0−8148∗	$12^h59^m02^s.9993$	−81°48′58″.678	–	–	–	–	–	–	–
J1303.1−4714∗	$13^h03^m09^s.071$	−47°14′17″.1533	59887.1354	68	126	147	60	5.3	23.9
J1345.9−2612∗	$13^h45^m55^s.5615$	−26°12′41″.7577	59835.6952	71	102	119	56	4.7	23.2
J1356.6+0234∗	$13^h56^m39^s.3347$	+02°34′38″.2803	–	–	–	–	–	–	–
J1400.0−2415	$14^h00^m04^s.9438$	−24°15′57″.6027	59835.7255	72	90	102	56	4.6	23.2
J1416.7−5023	$14^h16^m42^s.7441$	−50°23′22″.1988	59835.7475	88	115	133	56	9.8	28.4
J1450.8−1424	$14^h50^m50^s.592$	−14°24′21″.24	59835.7401	72	109	129	56	4.9	23.4
J1458.8−2120	$14^h58^m48^s.7903$	−21°20′19″.6815	59835.7619	74	90	100	56	5.6	24.1
J1513.7−1519	$15^h13^m46^s.6809$	−15°19′59″.1611	59835.7548	76	100	115	56	6.3	24.8
J1517.7−4446	$15^h17^m42^s.7185$	−44°46′36″.1166	59933.5247	88	151	181	60	12.2	30.8
J1526.6−3810	$15^h26^m38^s.2544$	−38°10′08″.3954	59835.809	91	137	161	56	11.0	29.5
J1527.8+1013	$15^h27^m53^s.0164$	+10°13′42″.9584	59835.7329	76	129	151	56	6.0	24.5
J1530.0−1522	$15^h30^m00^s.2637$	−15°22′33″.241	59933.5174	71	119	143	60	6.4	24.9
J1539.4−3323	$15^h39^m24^s.2651$	−33°23′55″.3226	59933.5031	77	85	91	60	8.4	27.0
J1543.6−0244	$15^h43^m37^s.8479$	−02°44′49″.5604	59978.0833	67	92	108	60	4.5	23.0
J1544.2−2554†	$15^h44^m12^s.5537$	−25°54′45″.0014	60102.9951	30	49	59	60	7.0	25.5
J1612.1+1407	$16^h12^m07^s.511$	+14°07′00″.4811	59835.7181	83	110	127	56	8.5	27.0

Downloaded from https://academic.oup.com/mnras/article/547/4/stag406/8501212 by guest on 05 May 2026

Table A2 – *continued*

4FGL NAME	R.A. (J2000)	Decl. (J2000)	MJD	$S_{\rm min}$ (μJy)	$S_{\rm med}$ (μJy)	S_{95} (μJy)	nAnt	$T_{\rm sky}$ (K)	$T_{\rm sys}$ (K)
J1622.2−7202	$16^{\rm h}22^{\rm m}12\overset{\rm s}{.}6013$	−72°02′23.″6462	59933.5967	69	87	100	60	5.5	24.0
J1630.1−1049	$16^{\rm h}30^{\rm m}06\overset{\rm s}{.}936$	−10°49′05.″8809	59933.532	73	102	121	60	7.0	25.5
J1641.3−2908	$16^{\rm h}41^{\rm m}21\overset{\rm s}{.}3611$	−29°08′21.″4778	59978.0904	84	152	174	60	10.6	29.1
J1646.7−2154	$16^{\rm h}46^{\rm m}44\overset{\rm s}{.}425$	−21°54′26.″9975	59978.0975	82	135	160	60	10.1	28.6
J1656.4−0410	$16^{\rm h}56^{\rm m}28\overset{\rm s}{.}656$	−04°10′12.″7195	59933.5536	73	95	110	60	6.8	25.4
J1659.0−0140	$16^{\rm h}59^{\rm m}03\overset{\rm s}{.}7207$	−01°40′39″	59933.5466	77	97	110	60	8.2	26.8
J1708.8−0923	$17^{\rm h}08^{\rm m}48\overset{\rm s}{.}0981$	−09°23′39.″4817	59978.1349	78	157	174	60	8.4	27.0
J1709.4−2127	$17^{\rm h}09^{\rm m}25\overset{\rm s}{.}3711$	−21°27′23.″0397	59933.5893	89	151	182	60	12.6	31.1
J1709.9−0900	$17^{\rm h}09^{\rm m}56\overset{\rm s}{.}0156$	−09°00′51.″8383	59933.5679	77	157	176	60	8.4	26.9
J1711.9−1922*	$17^{\rm h}11^{\rm m}54\overset{\rm s}{.}624$	−19°22′03.″3582	59978.1277	84	103	116	60	10.7	29.3
J1717.5−5804	$17^{\rm h}17^{\rm m}30\overset{\rm s}{.}813$	−58°04′14.″155	59933.6039	84	107	123	60	10.8	29.4
J1720.6+0708	$17^{\rm h}20^{\rm m}39\overset{\rm s}{.}3091$	+07°08′48.″8406	59835.7943	89	118	137	56	10.2	28.7
J1722.8−0418	$17^{\rm h}22^{\rm m}50\overset{\rm s}{.}7568$	−04°18′11.″8797	59933.575	78	94	105	60	8.8	27.3
J1727.4+0326	$17^{\rm h}27^{\rm m}27\overset{\rm s}{.}1436$	+03°26′59.″2801	59933.5608	78	103	120	60	8.7	27.2
J1730.4−0359	$17^{\rm h}30^{\rm m}26\overset{\rm s}{.}0669$	−03°59′32.″2801	59933.4959	82	103	117	60	9.8	28.3
J1735.3−0717	$17^{\rm h}35^{\rm m}21\overset{\rm s}{.}6211$	−07°17′07.″0792	59933.5822	86	127	152	60	11.5	30.1
J1739.1−1059	$17^{\rm h}39^{\rm m}08\overset{\rm s}{.}064$	−10°59′41.″2786	59978.1496	90	173	195	60	12.9	31.5
J1747.6+0324	$17^{\rm h}47^{\rm m}37\overset{\rm s}{.}2217$	+03°24′26.″28	59978.1645	86	105	121	60	11.3	29.9
J1749.8−0303	$17^{\rm h}49^{\rm m}50\overset{\rm s}{.}9253$	−03°03′06.″48	59978.1716	90	118	137	60	12.9	31.4
J1813.7−6846	$18^{\rm h}13^{\rm m}47\overset{\rm s}{.}5415$	−68°46′42.″6123	59978.112	70	103	121	60	5.8	24.3
J1816.4−6405*	$18^{\rm h}16^{\rm m}27\overset{\rm s}{.}5977$	−64°05′05.″9967	59978.1049	73	97	113	60	7.0	25.5
J1816.7+1749	$18^{\rm h}16^{\rm m}45\overset{\rm s}{.}0513$	+17°49′40.″4398	59835.8015	85	109	126	56	9.0	27.6
J1818.6+1316	$18^{\rm h}18^{\rm m}36\overset{\rm s}{.}6504$	+13°16′23.″1596	59933.5393	80	104	121	60	9.2	27.8
J1822.9−4718	$18^{\rm h}22^{\rm m}56\overset{\rm s}{.}6895$	−47°18′16.″9162	59978.1423	76	101	117	60	8.0	26.6
J1823.2+1209*	$18^{\rm h}23^{\rm m}14\overset{\rm s}{.}8828$	+12°09′26.″28	–	–	–	–	–	–	–
J1824.2−5427	$18^{\rm h}24^{\rm m}16\overset{\rm s}{.}897$	−54°27′05.″0427	59978.157	71	88	100	60	6.2	24.7
J1827.5+1141	$18^{\rm h}27^{\rm m}30\overset{\rm s}{.}8643$	+11°41′10.″681	59978.2075	86	103	121	60	11.3	29.9
J1831.1−6503*	$18^{\rm h}31^{\rm m}06\overset{\rm s}{.}5552$	−65°03′57.″2498	59835.7858	76	92	103	56	6.2	24.8
J1845.8−2521*	$18^{\rm h}45^{\rm m}51\overset{\rm s}{.}5552$	−25°21′30.″5983	59978.1788	91	123	143	60	13.0	31.5
J1906.0−1718	$19^{\rm h}06^{\rm m}04\overset{\rm s}{.}4604$	−17°18′55.″08	59978.1931	81	129	153	60	9.7	28.3
J1910.7−5320*	$19^{\rm h}10^{\rm m}47\overset{\rm s}{.}7393$	−53°20′18.″6035	59730.2738	75	143	163	60	5.8	24.3
J1913.4−1526	$19^{\rm h}13^{\rm m}24\overset{\rm s}{.}3604$	−15°26′58.″5608	59978.186	81	105	121	60	9.5	28.1
J1916.8−3025	$19^{\rm h}16^{\rm m}53\overset{\rm s}{.}6865$	−30°25′28.″5622	–	–	–	–	–	–	–
J1924.8−1035*	$19^{\rm h}24^{\rm m}49\overset{\rm s}{.}27$	−10°35′27.″2415	59978.2003	83	97	106	60	10.2	28.8
J1947.6−1121	$19^{\rm h}47^{\rm m}39\overset{\rm s}{.}8657$	−11°21′54.″7202	–	–	–	–	–	–	–
J2026.3+1431	$20^{\rm h}26^{\rm m}23\overset{\rm s}{.}7085$	+14°31′21.″0001	59933.6116	68	96	115	60	5.2	23.7
J2029.5−4237*	$20^{\rm h}29^{\rm m}30\overset{\rm s}{.}3589$	−42°37′42.″6068	–	–	–	–	–	–	–
J2043.9−4802	$20^{\rm h}43^{\rm m}55\overset{\rm s}{.}5615$	−48°02′23.″2755	59835.6874	72	89	100	56	5.0	23.5
J2112.5−3043	$21^{\rm h}12^{\rm m}33\overset{\rm s}{.}6035$	−30°43′45.″4784	59835.7701	71	77	81	56	4.4	23.0
J2121.8−3412	$21^{\rm h}21^{\rm m}53\overset{\rm s}{.}811$	−34°12′11.″8817	59786.1333	65	110	124	60	4.1	22.6
J2133.1−6432	$21^{\rm h}33^{\rm m}10\overset{\rm s}{.}8252$	−64°32′17.″8784	59835.6802	71	87	98	56	4.2	22.8
J2201.0−6928	$22^{\rm h}01^{\rm m}01\overset{\rm s}{.}6772$	−69°28′26.″0394	59786.1406	65	87	101	60	4.2	22.7
J2212.4+0708	$22^{\rm h}12^{\rm m}25\overset{\rm s}{.}9937$	+07°08′34.″0795	59786.1182	64	83	95	60	3.8	22.3
J2219.7−6837	$22^{\rm h}19^{\rm m}47\overset{\rm s}{.}2559$	−68°37′02.″287	59786.1259	64	80	90	60	3.9	22.4
J2241.4−8327	$22^{\rm h}41^{\rm m}25\overset{\rm s}{.}6348$	−83°27′40.″3088	59835.7028	70	91	107	56	4.2	22.7
J2355.5−6614*	$23^{\rm h}55^{\rm m}33\overset{\rm s}{.}7939$	−66°14′04.″1895	59835.71	69	92	109	56	3.9	22.4

Table A3. Initial information on slow pulsars. Note that the positions reported here correspond to approximate localization within the incoherent beam due to the lack of coherent beam detection, except for PSR J1303−4713, for which the position and uncertainties are from SEEKAT. The signal-to-noise ratios are measured from the discovery observations folded with PULSARX.

Name PSR	R.A. (J2000)	Decl. (J2000)	MJD	Spin frequency ν (Hz)	DM (pc cm^{-3})	Signal-to-noise ratio S/N
J1207−45	$12^{\rm h}07^{\rm m}(05)$	−45°36′(48)	59563.0596209787	2.10004(3)	23.76(20)	15.2
J1303−4713	$13^{\rm h}03^{\rm m}31\overset{\rm s}{.}5(5)$	−47°13′12.″8(4)	59887.1308713678	0.39014(1)	83.97(99)	16.5
J1816−64	$18^{\rm h}16^{\rm m}(07)$	−64°05′(48)	59786.0928676127	0.81840(1)	50.91(54)	14.3
J1845−25	$18^{\rm h}45^{\rm m}(04)$	−25°21′(48)	59786.0724193998	1.72310(2)	86.91(35)	10.5
J1924−10	$19^{\rm h}24^{\rm m}(03)$	−10°35′(48)	59978.1951990979	8.71501(2)	60.48(5)	16.4
J2355−66	$23^{\rm h}55^{\rm m}(08)$	−66°14′(48)	59563.0599451504	8.23064(1)	19.50(5)	11.7

Downloaded from https://academic.oup.com/mnras/article/547/4/stag406/8501212 by guest on 05 May 2026

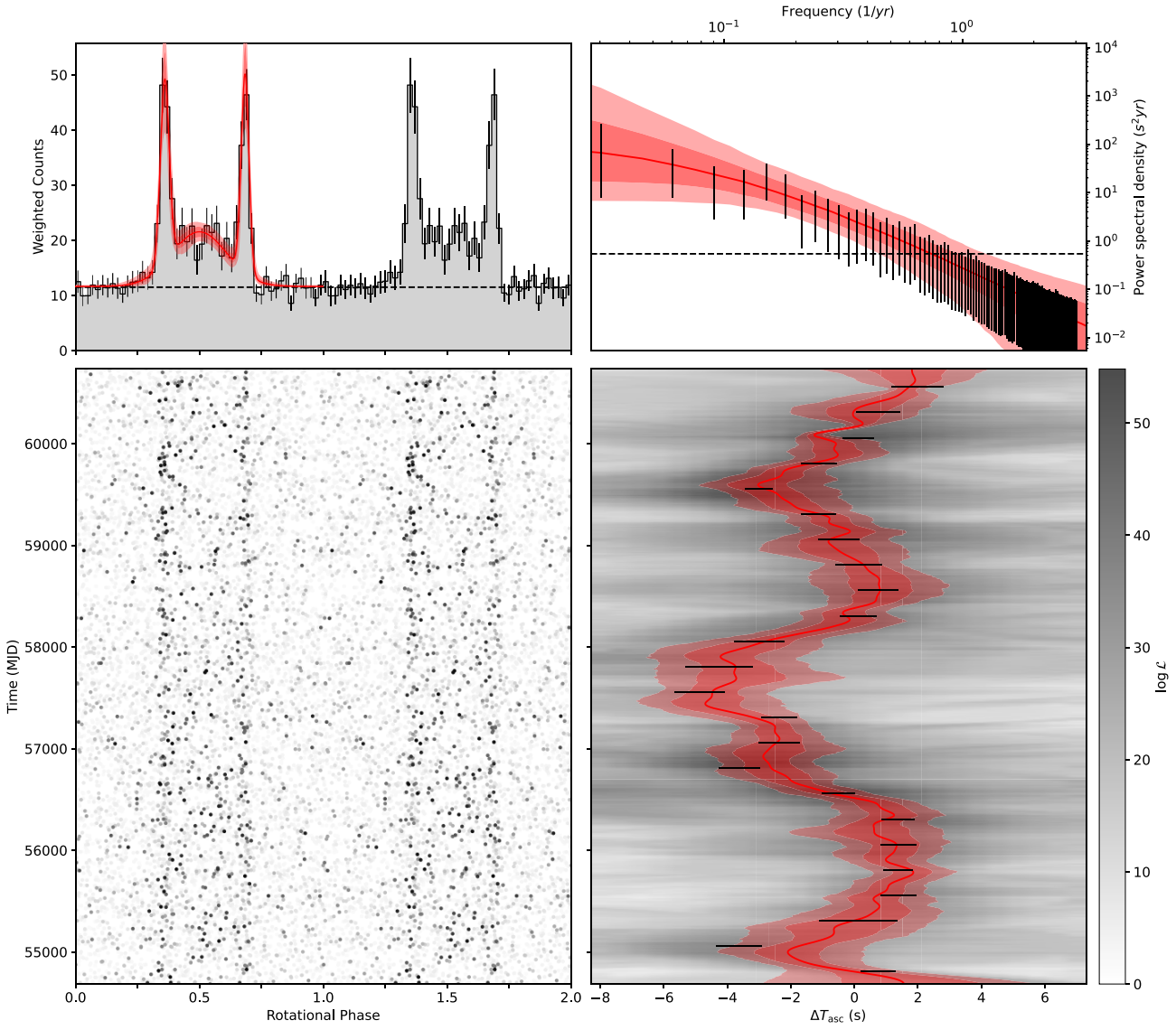

Figure B1. Gamma-ray pulsations and variations of the orbital phase over time for PSR J1831−6503. The panels on the left show the weighted pulsar spin phases of each gamma-ray photon for the highest-likelihood timing solution (bottom-left panel) and the integrated pulse profile (top-left panel). The red curve and the shaded regions represent the highest-likelihood pulse-profile template and the 1σ and 2σ template confidence intervals estimated from the Monte-Carlo samples. The bottom-right panel shows the orbital phase variations as a function of time. The grey-scale image shows the log-likelihood for offsets from the pulsar's T_{asc} as measured in overlapping 800-d windows, with 24 evenly spaced gamma-ray ToAs (black bars) to guide the eye. The red curve and shaded regions represent the solution used to fold the gamma-ray data and the 1σ and 2σ confidence intervals on those deviations, obtained from Monte-Carlo timing analysis. The top-right panel shows the power spectral density of the orbital phase variations. The black bars show the measured 1σ confidence interval on the power spectral densities. The red curve and shaded regions illustrate the highest-likelihood solution and the 1σ and 2σ confidence intervals of the Matérn model. The dashed line estimates the white-noise floor.

APPENDIX B: ORBITAL PERIOD VARIATIONS

Fig. B1 illustrates the gamma-ray pulsations and orbital phase variations for PSR J1831−6503.

[1]*Jodrell Bank Centre for Astrophysics, Department of Physics and Astronomy, The University of Manchester, Manchester M13 9PL, UK*
[2]*National Astronomical Research Institute of Thailand, Don Kaeo, Mae Rim, Chiang Mai 50180, Thailand*
[3]*Max Planck Institute for Gravitational Physics (Albert Einstein Institute), D-30167 Hannover, Germany*
[4]*Leibniz Universität Hannover, D-30167 Hannover, Germany*

Downloaded from https://academic.oup.com/mnras/article/547/4/stag406/8501212 by guest on 05 May 2026

[5]*INAF – Osservatorio Astronomico di Cagliari, Via della Scienza 5, I-09047 Selargius (CA), Italy*
[6]*Max-Planck-Institut für Radioastronomie, Auf dem Hügel 69, D-53121 Bonn, Germany*
[7]*South African Radio Astronomy Observatory, 2 Fir Street, Black River Park, Observatory 7925, South Africa*
[8]*NASA Goddard Space Flight Center, Code 662, Greenbelt, MD 20771, USA*
[9]*Department of Astronomy, University of Maryland, College Park, MD 20742, USA*
[10]*Center for Research and Exploration in Space Science & Technology II (CRESST II), NASA/GSFC, Greenbelt, MD 20771, USA*
[11]*National Radio Astronomy Observatory, 520 Edgemont Rd., Charlottesville, VA 22903, USA*
[12]*Center for Gravitation, Cosmology, and Astrophysics, Department of Physics, University of Wisconsin-Milwaukee, PO Box 413, Milwaukee, WI 53201, USA*
[13]*LAPTh, CNRS, USMB, F-74940 Annecy, France*
[14]*LPC2E, OSUC, Univ Orleans, CNRS, CNES, Observatoire de Paris, F-45071 Orleans, France*
[15]*ORN, Observatoire de Paris, Université PSL, Univ Orléans, CNRS, F-18330 Nançay, France*
[16]*Astrophysics Research Cluster, School of Mathematical & Physical Sciences, University of Sheffield, Sheffield S3 7RH, UK*
[17]*Instituto de Astrofisica de Canarias, E-38205 La Laguna, Tenerife, Spain*
[18]*School of Physics, Kane Building, University College Cork, Cork T12 K8AF, Ireland*

This paper has been typeset from a TEX/LATEX file prepared by the author.

Downloaded from https://academic.oup.com/mnras/article/547/4/stag406/8501212 by guest on 05 May 2026

© The Author(s) 2026.
Published by Oxford University Press on behalf of Royal Astronomical Society. This is an Open Access article distributed under the terms of the Creative Commons Attribution License (https://creativecommons.org/licenses/by/4.0/), which permits unrestricted reuse, distribution, and reproduction in any medium, provided the original work is properly cited.